Integration of GOCI and AHI Yonsei Aerosol Optical Depth Products During the 2016 KORUS-AQ and 2018 EMeRGe Campaigns

5 Hyunkwang Lim[1], Sujung Go[1,2], Jhoon Kim[1], Myungje Choi[2,3], Seoyoung Lee[1], Chang-Keun Song[4], Yasuko Kasai[5]

[1]Department of Atmospheric Sciences, Yonsei University, Seoul 03722, Republic of Korea
[2]Joint Center for Earth Systems Technology, University of Maryland Baltimore County, Baltimore, MD, USA
[3]Jet Propulsion Laboratory, California Institute of Technology, Pasadena, CA, USA
[4]School of Urban and Environmental Engineering, Ulsan National Institute of Science and Technology, Ulsan 44919,
10 Republic of Korea
[5]Natinal Institute of Information and Communications Technology, Tokyo 184-8759, Japan

Correspondence to: Jhoon Kim (jkim2@yonsei.ac.kr)

15 **Abstract.** The Yonsei AErosol Retrieval (YAER) algorithm for the Geostationary Ocean Color Imager (GOCI) retrieves aerosol optical properties only over dark surfaces, so it is important to mask pixels with bright surfaces. The Advanced Himawari Imager (AHI) is equipped with three shortwave-infrared and nine infrared channels, which is advantageous for bright-pixel masking. In addition, multiple visible and near-infrared channels provide a great advantage in aerosol property retrieval from the AHI and
20 GOCI. By applying the YAER algorithm to 10 minute AHI or 1 hour GOCI data at 6 km × 6 km resolution, diurnal variations and aerosol transport can be observed, which has not previously been possible from low-earth-orbit satellites. This study attempted to estimate the optimal aerosol optical depth (AOD) for East Asia by data fusion, taking into account satellite retrieval uncertainty. The data fusion involved two steps: (1) analysis of error characteristics of each retrieved result with respect to the
25 ground-based Aerosol Robotic Network (AERONET), and bias correction based on normalized difference vegetation indexes; and (2) compilation of the fused product using ensemble-mean and maximum-likelihood estimation methods. Fused results show a better statistics in terms of fraction within the expected error, correlation coefficient, root-mean-square error, median bias error than the retrieved result for each product.

30 # 1. Introduction

Aerosols are generated by human activities and natural processes on local to global scales, and have a lifetime of several to tens of days. Aerosols affect Earth's radiative energy balance by scattering and absorption (e.g. Cho et al., 2003). High aerosol loadings are persistent in Northeast Asia, including diverse aerosol types from various sources. Interactions among aerosols, clouds, and radiation in the

35   atmosphere cause significant uncertainties in climate-model calculations (IPCC, 2013). Datasets produced by satellites have been widely used to reduce such uncertainties (Saide et al., 2014; Pang et al., 2018), but the systems must be accurately calibrated, verified, and consistent. Satellite data have been used extensively to retrieve aerosol optical properties (AOPs) over broad areas, with several algorithms having been developed. Satellites in low earth orbit (LEO), including Sun-synchronous orbit (SSO),

40   cover the entire Earth over one to several days, depending on instrument and orbit characteristics. Most aerosol retrieval algorithms have been developed for LEO satellites (Kim et al., 2007; Lyapustin et al., 2011a, b; Lee et al., 2012; Fukuda et al., 2013; Hsu et al., 2013; Levy et al., 2013; Garay et al., 2017, 2020). LEO instruments currently onboard satellites include the Moderate Resolution Imaging Spectrometer (MODIS), Visible Infrared Imaging Radiometer Suite (VIIRS), Multi-angle Imaging

45   SpectroRadiometer (MISR), and Cloud and Aerosol Imager (CAI) (Remer et al., 2005; Lyapustin et al., 2011a, b, 2018; Fukuda et al., 2013; Hsu et al., 2013; Levy et al., 2013; Garay et al., 2017, 2020; Lee et al., 2017).

Representative algorithms developed for MODIS data include the Dark-Target (DT; Remer et al., 2005; Levy et al., 2013), Deep Blue (DB; Hsu et al., 2013; Sayer et al., 2014), and Multi-Angle

50   Implementation of Atmospheric Correction (MAIAC; Lyapustin et al., 2011a, b) systems, which are also applied for the succeeding VIIRS (Sayer et al., 2018). In the DT algorithm, the 2.1 μm channel is used to estimate land-surface reflectance in the visible (VIS) region using empirical equations based on the normalized difference vegetation index (NDVI). The DT algorithm has improved surface-reflectance modelling through consideration of the fractional area of urbanization (Gupta et al., 2016).

55   Ocean-surface reflectance is estimated using the Cox and Munk method (Cox and Munk, 1954), and AOPs over land and ocean are provided at spatial resolutions of 10 km × 10 km and 3 km × 3 km (Remer et al., 2013), respectively. The DB algorithm has an advantage over the DT algorithm in allowing aerosol data retrieval over bright surfaces. By using a shorter-wavelength channel, accuracy is improved over bright surfaces such as urban and desert areas, where surface reflectance was previously

60   estimated by the minimum reflectance method (MRM; Herman and Celarier 1997; Koelemeijer et al., 2003; Hsu et al., 2004). Furthermore, with the improvement to Collection 6.1, land-surface reflectance can be estimated similarly to the DT method, over densely vegetated regions (Sayer et al., 2019). In the case of VIIRS DB, aerosol retrieval over the ocean is also applied by the Satellite Ocean Aerosol Retrieval (SOAR) algorithm (Sayer et al., 2018). In the MODIS MAIAC system, surface reflectance is

65   estimated by considering various images based on time-series analysis, with multi-angle observations, based on up to 16 day data, and by applying the bidirectional reflectance distribution function (BRDF). Ocean-surface reflectance is determined using a Cox and Munk BRDF model similar to DT and VIIRS DB (Lyapustin et al., 2011a, b, 2018). The MISR observes Earth at nine different angles, providing a high degree of freedom in signals; consequently, retrievals yield estimates of aerosol type and shape. As

70   with the MAIAC, multiple observations are used, with the estimation of land-surface reflectance involving bidirectional reflectance factors (BRF). Zhang et al. (2016) developed an aerosol retrieval algorithm that allows aerosol data retrieval over bright land surfaces using surface-reflectance ratios from the VIIRS.

Aerosol retrieval algorithms for geosynchronous Earth orbit (GEO) satellites have been developed,

75   including the Geostationary Operational Environmental Satellite (GOES) series in the USA (Knapp et al., 2005), Meteosat series in Europe (Bernard et al., 2011), Himawari series in Japan (Yoon et al., 2007;

Kim et al., 2008; Lim et al., 2018; Kikuchi et al., 2018; Yoshida et al., 2018; Gupta et al., 2019), and the Geostationary Korea Multi-Purpose Satellite (GEO-KOMPSAT, GK) series in South Korea (Kim et al., 2014, 2016; Choi et al., 2016, 2018; Kim et al., 2020). However, previously launched geostationary
80 meteorological satellites had only a single, broadband VIS channel, with which it is difficult to retrieve AOPs other than aerosol optical depth (AOD) (Wang et al., 2003; Knapp et al., 2005; Kim et al., 2008, 2014, 2016; Bernard et al., 2011). However, the Geostationary Ocean Color Imager (GOCI) onboard the GK-1 satellite, also known as the Communication, Ocean, and Meteorological Satellite (COMS), has six VIS and two near-infrared (NIR) channels, which is advantageous for retrieving AOPs (Lee et al.,
85 2010; Choi et al., 2016, 2018; Kim et al., 2017). Next-generation meteorological GEO satellite instruments, including the Advanced Himawari Imager (AHI), Advanced Baseline Imager (ABI), and Advanced Meteorological Imager (AMI), have three to four VIS and NIR channels, which enable aerosol property retrieval with high accuracy (Lim et al., 2016, 2018; Kikuchi et al., 2018; Yoshida et al., 2018; Gupta et al., 2019). Kikuchi et al. (2018) and Yoshida et al. (2018) performed aerosol
90 retrievals using the MRM and corrected reflectance using empirical equations. Gupta et al. (2019) extended the MODIS DT algorithm to GEO satellites and estimated visible surface reflectance using SWIR reflectance. Lim et al. (2018) retrieved the AOPs using both MRM and estimated surface reflectance from short-wave IR (SWIR) data (estimated surface reflectance, ESR), and presented the two merged products: an L2-AOD merged product, and a reprocessed AOD produced by merging
95 MRM and ESR surface reflectances.

   Algorithms developed to date for LEO and GEO satellites have both advantages and disadvantages, depending on algorithm characteristics. Therefore, the MODIS team provides combined DT and DB AOD products (Levy et al., 2013; Sayer et al., 2014). In addition, several studies of the fusion of L2 products have been conducted (Levy et al., 2013; Sayer et al., 2014; Wei et al., 2019), with Bilal et al.
100 (2017) obtaining reliable results from merged DT and DB products, as indicated by the NDVI in East Asia, and also robust products by simply averaging DT and DB without consideration of the NDVI. AOP data fusion in East Asia may also be achieved using aerosol products of AMI, GOCI-2, and the geostationary environment monitoring spectrometer (GEMS) onboard the GK-2A and 2B satellites launched by South Korea in 2018 and 2020, respectively, with accuracy over bright surfaces being
105 improved by the GEMS aerosol product. It is also possible to obtain accurate AOPs, such as single-scattering albedo, aerosol loading height, and fine-mode fraction, which have been difficult to obtain by fusion of L2 data and/or surface reflectance data. If the trace-gas dataset retrieved from GEMS is used, it is possible to improve the aerosol type, with the retrieval of high-quality AOD data (Go et al., 2020).

   Several studies have considered AOD data fusion, for which methods can be broadly classified into
110 two types. First, the fusion of more than one AOD product may involve optimal interpolation (Xue et al., 2012), linear or second-order polynomial functions (Mélin et al., 2007), arithmetic or weighted means (Gupta et al., 2008), or maximum-likelihood estimates (MLE) (Nirala, 2008; Xu et al., 2015; Xie et al., 2018). Second, in the absence of satellite-derived AOD products for the day of fusion, the geostatistical fusion method, universal kriging method (Chatterjee et al., 2010; Li et al., 2014), geostatistical inverse
115 modelling (Wang et al., 2013), or spatial statistical data fusion (Nguyen et al., 2012) may be applied. These have the advantage that AOD can be estimated by integrating the spatial autocorrelation of AOD data even for pixels missing from the AOD products, although there is a disadvantage in not considering temporal correlations. The Bayesian maximum entropy (BME) method, taking into account temporal

autocorrelation, has also been developed (Tang et al., 2016). BME methodology can estimate gap-filling
120   pixels that are difficult to retrieve due to clouds, but with somewhat reduced accuracy. Gap filled AOD
using the BME method, and satellite-derived AOD discontinuity arises from insufficient temporal
sampling being available with the use of LEO satellites, resulting in a low fusion synergy. Previous
studies mentioned above include data fusion based on Kriging, reproduction of spectral AOD, and BME
method. Most of them focus on gap filling and rebuild AOD in areas not observed by MISR, MODIS,
125   and SeaWiFS, and so on (Wang et al., 2013; Tang et al., 2016). However in this study, we focused on
optimized AOD products with improved accuracy at the retrieved pixels by ensemble mean and MLE
fusion. We compared these two products, one very simple one and the other with more elaborated
processes. As previous AOD fusion studies improved the retrieved results mainly based on MLE or
NDVI-based fusion studies (Bilal et al., 2017; Levy et al., 2013; Wei et al., 2019; Go et al., 2020), we
130   tried to further improve them with efficient approach to save computation time considering the nature of
satellite data file size and user's near-real-time demand for data assimilation.
In this study, the GEO satellite dataset was used to resolve the temporal sampling issue for data fusion,
while maintaining the spatio-temporal resolution retrieved from GEO satellites. We also attempted to
estimate fused AOD products at 550nm with higher accuracy in East Asia. The ensemble-mean and
135   MLE methods were applied. Section 2 describes the two algorithms used in this study for AHI and
GOCI. Section 3 mentions methods of fusion and systematic bias correction, and section 4 performs
validation of the fused products with the Aerosol Robotic Network (AERONET) instruments during
two field campaigns: the Korea–United States Air Quality Study (KORUS-AQ) and the Effect of
Megacities on the Transport and Transformation of Pollutants on Regional and Global Scales Study
140   (EMeRGe).

2. Descriptions of AHI, GOCI, the YAER algorithm, and the two field campaigns

2.1 AHI aerosol algorithm

The Himawari-8 and -9 satellites were launched by the Japanese Meteorological Agency (JMA) on 7
October 2014 and 2 November 2016, respectively. The AHI onboard these satellites has 16 channels
145   covering wavelengths of 0.47–13.3 μm and performs full-disk and Japan-area observations every 10 and
2.5 min, respectively, from GEO at 140.7° E longitude (Bessho et al., 2016). Visible and NIR
observations are also performed at high spatial resolutions of 0.5–1.0 km, with SWIR to IR at 2 km,
which have advantages in aerosol property retrieval and cloud masking.
Lim et al. (2018) developed the AHI Yonsei aerosol retrieval (YAER) algorithm and provided two
150   retrieval results with 6 km × 6 km resolution at 550 nm based on MRM and ESR using SWIR data.
Aerosol property retrieval using VIS channels requires accurate surface reflectance, for which MRM
and ESR are useful, with the main difference between the two lying in the surface-reflectance
estimation method.
The MRM applies the minimum-reflectance technique over both land and ocean (Lim et al., 2018),
155   with surface reflectance being estimated by finding the minimum reflectance in each pixel over the past
30 day window, giving the Lambertian equivalent reflectance (LER; Knapp et al., 2002; Wang et al.,

2003; Kim et al., 2008; Choi et., 2016, 2018; Kim et al., 2016; Lim et al., 2018). This method takes the bidirectional characteristics of surface reflectance into consideration by obtaining surface reflectance at each observation time over the 30-day search window. However, the method assumes that during the search window there is more than one clear day and that surface reflectance does not change; otherwise, it is affected by clouds and/or the background aerosol optical depth (BAOD; Kim et al., 2014; Kim et al., 2021).

According to the ESR method, land-surface reflectance in the Vis region is constructed from the Top of Atmosphere (TOA) reflectance at 1.6 μm wavelength, based on the NDVI for SWIR and the fraction of urbanization and cropland (Levy et al 2013; Gupta et al., 2016; Zhong et al., 2016; Lim et al., 2018). Ocean-surface reflectance is estimated from the Cox and Munk BRDF model (Hsu et al., 2004; Lee et al., 2012; Jackson et al., 2013; Choi et al., 2016, 2018; Lim et al., 2018; Sayer et al., 2018). Chlorophyll-a concentrations are considered in addition to data from Japan Aerospace Exploration Agency (JAXA) (Murakami et al., 2016) and interpolated for the 10-min AHI intervals. For unretrieved pixels, the less contaminated chlorophyll-a concentration value of 0.02 mg m^{-3} is used. Details of the methodology can be found in Lim et al. (2018).

The MRM gives better accuracy over brighter surfaces such as urban areas, while the ESR method gives better accuracy over areas of dense vegetation (Lim et al., 2018). However, there is a critical surface reflectance at which aerosol signals disappear, depending on the single-scattering albedo (Kim et al., 2016). Over the ocean, both the MRM and ESR methods give high accuracy, but ESR results are robust with the Cox and Munk model.

The MRM requires more computational time than the ESR method to estimate surface reflectance, as it requires data for the past 30 days, and LER needs to be calculated using a radiative transfer model. The ESR method estimates surface reflectance from the observed TOA reflectance at 1.6 μm wavelength using empirical equations including the NDVI. The advantage of MRM is that stable surface reflectance values can be obtained regardless of surface type. However, due to the influence of BAOD, surface reflectance tends to be overestimated, with satellite-derived AOD data thus being underestimated (Kim et al., 2014). On the other hand, the ESR method uses TOA reflectance at 1.6 μm wavelength to detect surface signals, which is less sensitive to fine particles and BAOD. However, when aerosols such as yellow dust with coarse particles are transported from the Taklamakan and Gobi deserts, the BAOD effect also applies to the ESR method. The ESR method is also more likely to be affected by snow surfaces than the MRM, as snow reduces reflectivity around the 1.6 μm wavelength (Negi and Kokhanovsky, 2011). The ESR method also has the disadvantage of giving noisy results over bright surfaces such as desert. However, its fast surface-reflectance estimation enables near-real-time retrieval based on the AHI YAER algorithm.

2.2 GOCI aerosol algorithm

GOCI is an ocean color imager launched onboard COMS in 2010 and observes the East Asia region at an hourly interval with 500 m× 500 m resolution (Choi et al., 2012). It has eight bands in the VIS and NIR regions, which is advantageous for aerosol retrieval. Two versions of GOCI Yonsei aerosol algorithms have been developed, referred to as V1 and V2 (Lee et al., 2010; Choi et al., 2016, 2018). In the case of V1, surface reflectance is estimated by the MRM using LER for the past 30 days over land,

and the Cox and Munk BRDF model over oceans. In V2, ocean-surface reflectance is estimated by the same method, but land-surface reflectance is improved by using an accumulated long-term database. To minimize the impact of BAOD (the weakness of the MRM), a monthly surface-reflectance database was constructed using all of the LERs over the past five years, but it cannot reflect unexpected changes in surface conditions. However, a well-established climatological database allows aerosol property retrieval in near-real-time with reasonable accuracy.

3. Data fusion methods

Satellite-derived AODs have different error characteristics depending on NDVI, scattering angle, and so on (Choi et al., 2016, 2018; Lim et al., 2018). Over oceans, ESR AODs are more accurate than MRM AODs. However, the accuracy of GOCI, according to NDVI, has a negative bias for V1 and mostly a positive bias for V2 (Choi et al., 2018). In this study, we developed optimal AOD products at 550nm in East Asia by fusing four individual retrievals, i.e. two AHI aerosol products from the MRM and ESR methods, and two GOCI products from V1 and V2.

3.1 Spatio-temporal matching

The AHI and GOCI have different spatial pixel locations and temporal resolutions, so it is necessary to match their spatio-temporal resolutions before data fusion. GOCI and AHI AODs have the same spatial resolution of 6 km × 6 km, but the two satellites are located at 128.2° E and 140.7° E, respectively, at the equator. Spatial pixel matching is therefore required. However, satellite-derived AOD represents total-column extinction, so AOD retrieved by the two sensors is not significantly affected by satellite position. To merge the different satellite spatial pixel coverages, the GOCI pixel was re-gridded to match AHI pixels for full-disk observation, with up to 4 GOCI AOD pixels being used with average values considered representative of pixel values. If more than half of the AHI AOD pixels did not exist out of the maximum 6 AHI data per hour, it is regarded as cloud contaminated pixels and an additional cloud removal process is performed. This process applies to both the MRM and ESR method, to remove the AHI's additional cloud-contaminated pixels in products of both GOCI V1 and V2, which have a disadvantage in cloud masking due to their lack of IR channels. When three or more pixels were available for generating AHI data at 1 hour intervals, hourly AOD values were estimated as the medians of pixel values.

3.2 Ensemble mean method

Here, AMR represents AHI MRM AOD, AES represents AHI ESR AOD, GV1 represents GOCI V1 AOD, and GV2 represents GOCI V2 AOD. We performed data fusion using AMR, AES, GV1, and GV2 data within 1 hour intervals for which additional-cloud masking was performed. The ensemble mean is the mean of the ensemble member over a specific time. The ensemble members are AMR, AES, GV1, and GV2 based on two satellite instruments and two different surface-estimation methodologies. Table 1 provides the satellite-derived AOD used for ensemble-mean and MLE fusion.

Fusion was performed only when a pixel of an ensemble member was used for all fusions. Fusion 1 (F1) included the two AHI products of AMR and AES, and two GOCI products of GV1 and GV2. Fusion 2 (F2) involved the calculation of the YAER algorithm by the fusion of AES and GV2, both of which have the advantage of producing data in near-real-time. Fusion 3 (F3) merged AMR and AES to estimate AOD over a wide area, and Fusion 4 (F4) involved a comparison with F1 to determine how accuracy varied with decreasing number of ensemble members.

3.3 MLE method

Also, Table 1 shows the FM1 is the result of MLE fusion involving all satellite-derived AOD, and FM2 involves AER and GV2 for near-real-time operation. FM3 includes AMR and AES, enabling wide-area (70°-150 °E, 0°-50°N) observation.

The MLE method provides a means of weighting and averaging based on errors evaluated with AERONET ground-based measurements (Nirala, 2008; Xu et al., 2015; Xie et al., 2018). This method employs the following equations:

$$\tau_i^{MLE} = \sum_{k=1}^{N} \frac{R_{i,k}^{-2}}{\sum_{k=1}^{N} R_{i,k}^{-2}} \tau_{i,k} \qquad (1)$$

$$R_{i,k} = \sqrt{\frac{\sum_{i=1}^{M}(s_{i,k} - g_i)^2}{M}} \qquad (2)$$

where τ_i^{MLE} represents the fused AOD; $\tau_{i,k}$ represents the mean AOD at grid point i from the satellite-derived AOD product k, where k is the index for different satellite-derived AOD products for fusion; $R_{i,k}$ represents the root-mean-square error (RMSE) at grid point i for the satellite-derived AOD product k; N is the number of all AOD data; g_i represents the mean of ground-based AOD at grid point i from the AERONET (collocated temporal mean); $s_{i,k}$ represents the mean of satellite derived AOD products (k) at grid points of the AERONET (collocated spatial mean); and M is the number of pairs of $s_{i,k}$ and g_i.

Satellite observation can cover wide areas, but the ground observation instrument cannot cover all satellite observed areas. Therefore, a RMSE model was constructed for AOD, time, and NDVI through comparative validation with AERONET observation as shown in Figure 1. For MLE over wide areas without ground measurements, the calculated RMSE from AOD, time, and NDVI bins was applied for every satellite pixel. We excluded points that AOD differences with respect to AERONET data (dAOD) were > 2 standard deviations (SD) to remove outliers and to consider only the more stable RMSE values.

3.4 Bias correction

AOD follows a log-normal distribution (Sayer and Knobelspiesse, 2019), but dAOD for each satellite product follow a Gaussian distribution (Sayer et al., 2013). The quantile–quantile (Q-Q) plot is a graphical statistical technique that compares two probability distributions with each other. The x-axis represents the quantile value of the directly calculated sample, and the y-axis represents the Z-score. Here, the Z-score is a dimensionless value that makes a statistically Gaussian distribution and shows where each sample is located on the standard deviation. That is, when Z-score is 1 and 2 represent 1 SD and 2 SD, respectively. In addition, as the Q-Q plot shows a linear shape, the sample follows a Gaussian distribution.

Figure 2 shows dAOD analyzed for each satellite product, for the analysis period from April 2018 to March 2019, excluding the EMeRGe campaign. In the Q-Q plot, the overall linear relationship is well represented within 1 SD. There is no linear relationship between 1 SD (black solid line) and 2 SD (black dotted line), but soon again appears in a linear relationship.

To minimize the effect of outliers in this process, data beyond 2 SD were excluded and applied differently according to NDVI and time. Data beyond 2 SD of dAOD were excluded to prevent a change in bias trends due to AOD errors caused by cloud shadows and pixels contaminated by clouds. Bias correction values are provided in Figure 3 where Gaussian center is calculated differently for NDVI, time, and respective satellite products, through the Gaussian fitting of the dAODs. Through this process of shifting the obtained Gaussian center values to match the 0 in bias, the systematic bias of the algorithms was corrected. This process was performed before applying the MLE method, which allows compensation for systematic bias that is difficult to obtain directly in MLE.

3.5 Evaluation of aerosol products during two field campaigns

The performance of fused products was analyzed in two field campaigns: the KORUS-AQ of 1 May 2016 to 12 Jun 2016 (https://www-air.larc.nasa.gov/missions/korus-aq/), and the EMeRGe of 12 Mar 2018 to 8 Apr 2018 (https://www.halo.dlr.de/science/missions/emerge/emerge.html). KORUS-AQ was an international multi-organization mission to observe air quality across the Korean Peninsula and surrounding waters, led by the US National Aeronautics and Space Administration (NASA) and the Korean National Institute of Environmental Research (NIER). EMeRGe aimed to investigate experimentally the patterns of atmospheric transport and transformation of pollution plumes originating from Eurasia, tropical and subtropical Asian megacities, and other major population centers. GEO satellite data played an important role in these campaigns; e.g., data assimilation for chemical transport models and tracking aerosol plumes (Saide et al., 2014, 2010; Pang et al., 2018). Here, we applied satellite-derived GOCI and AHI AODs, with a spatial resolution of 6 km × 6 km, and temporal resolutions of 1 hour and 10 minutes, respectively.

4. Results

300   Figure 4 (a) shows the average AOD of FM1 (MLE method with all products) during the KORUS-AQ period, and Figure 4 (b-k) shows the respective difference in the average AOD of AMR, AES, GV1, GV2, F1, F2, F3, F4, FM2, and FM3 with respect to FM1. The result of the comparison with the respective satellite product (Figure 4 (b-e)) shows different features. AMR shows a negative bias over the ocean but shows similar results to FM1 over land, while AES shows a different tendency in northern

305   and southern China. GV1 tends to show opposite pattern to AES, and GV2 shows positive bias over the ocean and results in similar pattern to FM1 over the land. In the west of the Korean peninsula, AES AOD is overestimated compared to FM1. Although the AES algorithm considers the fraction of urbanization, there is still a tendency to overestimate AODs. The main reason why AES results show different patterns is the different estimation process of the land surface reflectance from that of other

310   products.
      On the other hand, in GV1, the AOD over the Manchurian region is overestimated. This is because the aerosol signal is small over bright surface, making it difficult to retrieve aerosol properties. These features tend to be alleviated in GV2, where the surface reflectance and cloud removal process were improved. Also, the difference was the least for the F1 result that differs only in the fusion method

315   under the same configuration as FM1, and the F4 result (AMR, AES, and GV2) showed similar results. F3 and FM3, fusion products using AHI only, retain relatively strong AES features, thus their differences from FM1 (Figure 4 (h) and (k)) showing similar pattern as AES cases in Figure 4 (c).
      Figure 5 shows the same result as Figure 4 except for the EMeRGe period. The AMR and AES overestimated AODs in northern China, which is thought to be the snow contaminated pixel. The

320   EMeRGe period was in March-April, when northern China is more covered by snow compared to the KORUS-AQ period in May-June. On the other hand, for GV1 and GV2, the effect of overestimation with snow contaminated pixel is relatively small, as their snow masking is well performed. However, for the KORUS-AQ period, it seems that the GV1's overestimation of AOD in northern China still remains. FM1, the MLE product of F1, showed the most similar results naturally, followed by F4.

325   However, since this analysis (Figure 4 and 5) is a fusion between the three MRM results and one ESR result, the average field difference is naturally the largest in AES which uses ESR method.
      For the characteristics of the average AOD for the two campaign period, high AODs during the KORUS-AQ period were found in eastern China, and Hokkaido as wildfires from Russia were transported to Hokkaido (Lee et al., 2019). Meanwhile, during the EMeRGe period, high AOD is shown

330   over the Yellow sea as aerosols were transported from China to the Korean peninsula through the west coast, contrary to the KORUS-AQ period. Overall, the average AODs for the EMeRGe are less smooth than those of the KORUS-AQ period. This is because the EMeRGe period was shorter than that of the KORUS-AQ, and the retrieval accuracy was lower due to the bright surface.

335   The Gangneung-Wonju National University site (Gangneung-WNU; 128.87°E, 37.77°N) lies on the eastern side of the Korean Peninsula and it is one of the regions with low aerosol loadings. The AOD frequency distribution generally follows a log-normal distribution, and it is important to estimate low AOD levels exactly to increase its accuracy. Therefore, we evaluated whether the fused products were improved at low AODs. A time-series comparison of different satellite AOD products with AERONET

340 (on a logarithmic scale) is shown in Figure 6 for the Gangneung-WNU site without high AOD events, where most point AERONET AODs at 550 nm were < 1 during the KORUS-AQ campaign. Time-series data from ground instrument, AMR, AES, GV1, and GV2 products are shown in Figure 6 (a), where black filled circles represent AERONET AOD as ground-truth data, and satellite-derived AODs (in different colors) show similar variabilities. AMR, GV1, and GV2 products based on the MRM generally
345 exhibit negative biases, with AES AODs being higher than other products. Ensemble-mean and MLE results are presented in Figure 6 (b) and (c), respectively, and show better agreement with the AERONET AOD than individual satellite AOD. This can also be seen from the dAOD indicated as solid line in Figure 6, where errors become smaller by going through the fusion process.

   MLE results, which consider pixel-level uncertainties (in contrast to ensemble means), are superior in
350 following the variability of ground-based AERONET observations, even at low AODs. The MLE products were implemented in a way to improve accuracy for the low AOD region more critically than in the high AOD region by systematic bias correction. Surface reflectance estimated by the MRM is affected by BAOD, and AOD thus shows a negative bias. On the other hand, the AER uses TOA reflectance at 1.6 µm wavelength to estimate surface reflectance and is therefore less affected by BAOD,
355 and shows higher AOD than AMR and the two GOCI AODs. Furthermore, AOD retrieval over vegetated areas is more accurate with the ESR method. This result is consistent with previous studies of aerosol retrieval in the VIS region (Levy et al., 2013; Gupta et al., 2019; Hsu et al., 2019).

5. Error estimation and validation against AERONET

360   For validation and error estimation, AERONET aerosol products were used for ground truth. AERONET offers freely available spectral AOD measurements every 15 min (or less) at numerous monitoring sites worldwide, with an uncertainty of 1%–2% under cloudless conditions (Smirnov et al., 2000; Holben et al., 2001). Newly updated AERONET Version 3 Level 2.0 AOPs with additional cloud screening and quality control were selected for validation purposes (Giles et al., 2019). The number of
365 AERONET sites used for validation in this study, was 69 and 35 during the KORUS-AQ campaign, and 55 and 21 during the EMeRGe campaign, for AHI and GOCI, respectively.

5.1 Validation with AERONET

   Spatio-temporal correlation between satellite-derived AOD and AERONET AOD involved data
370 averaged over all satellite pixels within a 25 km radius of the AERONET site, and AERONET AOD averaged over ±30 minutes from the satellite observation time. As validation metrics, Pearson's correlation coefficient, mean absolute error (MAE), median bias error (MBE), and the fraction (%) within the expected error (EE) were applied. The MODIS DT algorithm provided EE as $\pm0.05 \pm 0.15 \times$ AOD (Levy et al., 2010). Results of the comparison with AERONET during the KORUS-AQ are shown
375 in Figure 7, the EE values of AER, AES, G1, and GV2 were 53.2%, 58.0%, 52.2%, and 50.3%, respectively. Fused products have EE values of up to 73.3%, much higher than the respective satellite product. In terms of RMSE, all of the fusion products without F3 and FM3 (validation over a broader

area) have a value of 0.128, lower than the minimum value of various satellite products (0.153). Figure 7 (g) and (k) shows relatively scattered patterns compared with other fusion products because they show data fused with only AHI products. EE values for all AERONET products used for validation are shown in Figure 8, where AHI covers a broader area than GOCI. The accuracy is low over northern India and the Indochina Peninsula. However, EE values after fusion (Figure 8 (g, k)) are higher than those of the respective satellite product. The fused results (Figure 8 (g, k)) of two AHI products display high EE values within the domains of GOCI and other fusion products. The scattered fusion results based on two AHI products (Figure 7) can thus be attributed to issues at these particular sites, rather than to the satellite products themselves. Results of the comparative validation with AERONET during the EMeRGe campaign (Figure 9) indicate that, overall, fusion products improve the statistical metrics, as in the KORUS-AQ case. The validation result for each satellite product shows that the maximum value of EE is 63.4%–68.0% after fusion. Thus, the EE increases as other statistics improve, including an RMSE decrease from 0.162 to 0.149. However, despite the MLE fusion (FM1-3) with bias correction using the Gaussian center values, MBE shows a rather poor result. This is because the Gaussian center value used for error correction does not work properly during the EMeRGe campaign. Low NDVI in summer is generally seen for bright surfaces such as deserts, but low NDVIs are present in many areas, other than deserts during the EMeRGe campaign period. To improve this, it is desirable to use seasonal Gaussian center values.

As in the KORUS-AQ campaign, the validation results for the two AHI products and the fusion products based on AHI AODs only are inferior to the results for the fusion products based on GOCI AODs. This is because the validation was performed over wider areas, and problems were noted at specific sites. The fused results showed improved accuracy not only in terms of EE but also in statistical metrics such as RSME, MBE, and MAE. Results for the EMeRGe campaign are shown in Figure 10. During that campaign, validation results over brighter surfaces in northern India and the Indochina Peninsula show reduced accuracy, but fusion results show consistently higher EE values than individual satellite products.

5.2 Error estimation

Differences between satellite products and AERONET, dAOD values were analyzed on the basis of NDVI values and observation times (Figure 11). Figure 11 (a) and d shows the respective satellite products, Figure 11 (b) and (c) the ensemble-mean product, and Figure 11 (c) and (f) the MLE fusion results, with each filled circle representing the mean of 800 and 600 collocated data points sorted in terms of NDVI for the KORUS-AQ and the EMeRGe campaigns, respectively. Figure 11a shows different biases for each satellite product, with AMR and GV1 being negative, AES positive, and GV2 converging to almost zero. The errors are close to zero for both the ensemble-mean and MLE products as a result of the fusion process. During the EMeRGe campaign (right column, Figure 11), the two AHI and two GOCI products show negative biases, and even the ensemble-mean results have negative biases. The ensemble mean does not include any bias correction, meaning that the error characteristics of each original satellite product are intact. The MLE products display improved biases in terms of NDVI, which are close to zero because the bias was corrected for in the MLE process.

The median bias of the AOD products over the observation time was analyzed as shown in Figure 12 where the left column represents the KORUS-AQ and the right column the EMeRGe campaign, with filled circles representing median values, and the error bar being ±1 SD. As in the KORUS-AQ
420 campaign, the AMR shows a generally negative bias, as in the all-time results, and a negative bias also exists in each time zone. However, the AES shows a positive bias. In the GOCI case, positive and negative biases appear differently according to time zones. In the EMeRGe period, the two AHI results have large error ranges. GEO satellites perform observations over a specific area with a fixed viewing zenith-angle and retrieve AOPs by solar reflectance, which means that a specific site has different local
425 time depending on its longitude for a given satellite image. Furthermore, there are fewer data for the EMeRGe period than the KORUS-AQ period, and data for northern India and the Indochina Peninsula, which have low accuracy, are included in the data for 0100–0300 UTC, indicating large errors. In the KORUS-AQ period, the data fraction for a specific site is not as large as in the EMeRGe period, so this problem does not arise.
430 Taylor diagrams for accuracy evaluation of AOD data fusion products are shown in Figure 13. The Taylor diagram is a graphic summary of how closely satellite retrievals match observations. Here, match-up values were respective and fusion AOD products, and the matching up data were AERONET AOD. Correlation coefficient, SD, RSME, and EE values were used as the matching criteria. The correlation coefficient is shown in green (Figure 13) with a polar angle, the SD is shown in the radial
435 distance on the black x- and y-axes, and RMSE is the proportional cyan circle from the "AERONET" point on the x-axis. The EE value, which can evaluate the stability of AODs, is shown for each color. AMR, AES, GV1, GV2, F1, F2, F3, F4, FM1, FM2, and FM3 are indicated by different symbol, respectively.
Correlation coefficients are all around 0.8–0.9 with no significant differences for respective and fusion
440 AODs. However, results after fusion show slightly better than respective satellite product accuracy in terms of SD, RMSE, and EE values.
Standard deviation values indicate that products that lie outside the purple dotted half-circle are larger than the SD of AERONET. In the AHI case, the SD appears smaller than GOCI values because it tends to underestimate values at high AOD. Similarly, RMSE values are lower after fusion.
445 The EMeRGe period was from March to April, when the surface is brighter in East Asia than during the KORUS-AQ period of May to June. The accuracy during the EMeRGe period is therefore similar to or slightly poorer than that of the KORUS-AQ period. The correlation coefficient shows similar values, but the SD, RMSE, and EE values are slightly lower. Again, the accuracy of the validation metrics is improved by fusion.
450 The error analysis indicates that the results after fusion are more accurate than the results obtained using individual satellite product, and accuracy was slightly better during KORUS-AQ than EMeRGe because more data points were considered. Also, the surface was relatively dark during the KORUS-AQ period, thus reduced errors for aerosol retrieval than during the EMeRGe period.

5.3 Accuracy evaluation for AHI products of GOCI domain

In this section, the accuracy of AHI products in the GOCI domain was evaluated. Table 2 shows all sites and co-located sites with GOCI for AMR, AES, F3, and FM3, where values exist for a wide area, and summarizes them for the KORUS-AQ and the EMeRGe periods. First, during the KORUS-AQ period, it can be seen that the number of collocated data has decreased by about 2000 points. By reducing the validation area, R, RMSE, MBE, and %EE were improved. RMSE is 0.150 and 0.145, which is better than 0.153 and 0.176 of GV1 and GV2, and there is a difference of more than 10% in %EE. Likewise, the results of fusion products are also improved.

However, there is a slightly different trend for the EMeRGe period. First of all, by reducing the area, the percentage of reduced points is more than 60%, which is more than the 30% for the KORUS-AQ period. In existing AMR and AES products, the statistical value tends to increase as the area becomes smaller. However, the fusion product's accuracy is rather decreased for the GOCI coverage. For AMR and AES, MBE and RMSE are similar to or better than GV1 and GV2, and %EE are higher than GV1 and GV2. However, in contrast to the KORUS-AQ period, the bias characteristics of AMR and AES are also negative, so the accuracy of F3 is inferior to the existing products. Meanwhile, the decrease in the accuracy of the FM3 product can be explained by difficulty to obtain accurate statistics due to higher weight in other areas beyond GOCI domain.

6. Summary and conclusion

Various aerosol algorithms have been developed based on two different GEO satellites, AHI, and GOCI. Retrieved AOD data have advantages and disadvantages, depending on the concept of the algorithm and surface-reflectance estimations. In this study, four aerosol products (GV1, GV2, AMR, and AES) were used to construct ensemble-mean and MLE products. Based on the ensemble mean, this study presented fusion products taking advantage of overlap region, accuracy, and near-real-time processing, as well as MLE products including pixel-level errors. Bias corrections for different times were performed while considering pixel-level errors, and the synergy of fusion between GEO satellites demonstrated.

Validation with the AERONET confirmed that consideration of pixel-level uncertainty improved the accuracy of MLE products. The accuracy after fusion was better than that of individual satellite product. The %EE of each satellite-derived product during the KORUS-AQ was 53.2%, 58.0%, 52.2%, and 50.3% in AMR, AES, GV1, and GV2; and the RMSE was 0.180, 0.201, 0.153, and 0.176, respectively. After the ensemble-mean process, the EE of F1, F2, F3, and F4 increased to 67.8%, 72.3%, 63.5%, and 73.3%, respectively. FM1, FM2, and FM3, which are results of MLE fusion, had %EE values of 71.5%, 65.6%, and 65.0%, with RMSE values of 0.131, 0.148, and 0.161, respectively, better than the respective satellite product. Similarly, the EMeRGe period displayed better statistical values after fusion, with EE and RMSE values of 68.0% and 0.149, respectively. To provide optimized AOD products for East Asia, NDVI and time-dependent errors have been reduced. The ensemble mean and MLE fusion results show

better accuracy, and both show consistent results, indicating that there is no significant difference from the mean AOD in Figures 4(f) and 5 (f).

However, since both satellite algorithms retrieved AOPs through VIS channels, there remains an issue
495 of reduced accuracy over brighter surfaces, with AOP retrieval in the VIS channel being more accurate over dark surfaces, and with results being more accurate during the KORUS-AQ period than the EMeRGe period. The fusion products improved the accuracy of satellite products, and MLE products also improved the accuracy by taking into account pixel-based errors based on long-term data analysis. The method applied in this study could be used for AOD fusion of GEO data, such as AMI onboard
500 GK-2A, and GOCI-2 and GEMS onboard GK-2B. Furthermore, it is possible to retrieve AOPs other than AOD using multi-angle, multi-channel (UV, VIS, and IR) observations with GK-2A and 2B.

Code and data availability.

505

The aerosol products data from AHI and GOCI are available on request from the corresponding author (jkim2@yonsei.ac.kr).

Author contributions.

510

HL, SG and JK designed the experiment. HL and SG carried out the data processing. MC, SL, and YK provided support on satellite data. HL wrote the manuscript with contributions from co-authors. JK reviewed and edited the article. JK and CK provided support and supervision. All authors analyzed the measurement data and prepared the article with contributions from all co-authors.

515
Competing interests.

The authors declare that they have no conflict of interest.

520 **Acknowledgements**

We thank all principal investigators and their staff for establishing and maintaining the AERONET sites used in this investigation. This subject is supported by Korea Ministry of Environment (MOE) as "Public Technology Program based on Environmental Policy (2017000160001)". This work was also supported by a grant from the National Institute of Environment Research (NIER), funded by the
525 Ministry of Environment (MOE) of the Republic of Korea (NIER-2020-01-02-007). This research was also supported by the National Strategic Project-Fine particle of the National Research Foundation of Korea (NRF) funded by the Ministry of Science and ICT (MSIT), the Ministry of Environment (ME), and the Ministry of Health and Welfare (MOHW) (NRF-2017M3D8A1092022). We thank all members of the KORUS-AQ science team for their contributions to the field study and the data processing
530 (doi:10.5067/Suborbital/KORUSAQ/DATA01).

References

Bernard, E., Moulin, C., Ramon, D., Jolivet, D., Riedi, J., and Nicolas, J. M.: Description and validation of an AOT product over land at the 0.6 μm channel of the SEVIRI sensor onboard MSG, Atmospheric Measurement Techniques, 4, 2543-2565, 2011.

Bessho, K., Date, K., Hayashi, M., Ikeda, A., Imai, T., Inoue, H., Kumagai, Y., Miyakawa, T., Murata, H., Ohno, T., Okuyama, A., Oyama, R., Sasaki, Y., Shimazu, Y., Shimoji, K., Sumida, Y., Suzuki, M., Taniguchi, H., Tsuchiyama, H., Uesawa, D., Yokota, H., and Yoshida, R.: An Introduction to Himawari-8/9— Japan’s New-Generation Geostationary Meteorological Satellites, Journal of the Meteorological Society of Japan. Ser. II, 94, 151-183, 2016.

Bilal, M., Nichol, J. E., and Wang, L.: New customized methods for improvement of the MODIS C6 Dark Target and Deep Blue merged aerosol product, Remote Sensing of Environment, 197, 115-124, 2017.

Chatterjee, A., Michalak, A. M., Kahn, R. A., Paradise, S. R., Braverman, A. J., and Miller, C. E.: A geostatistical data fusion technique for merging remote sensing and ground-based observations of aerosol optical thickness, Journal of Geophysical Research, 115, 2010.

Cho, Hi K., Jeong, M. J., Kim, J., Kim, Y. J.: Dependence of diffuse photosynthetically active solar irradiance on total optical depth, Journal of Geophysical Research, 108, D9, 4267, 4-1~4-10, 2003.

Choi, J.-K., Park, Y. J., Ahn, J. H., Lim, H.-S., Eom, J., and Ryu, J.-H.: GOCI, the world's first geostationary ocean color observation satellite, for the monitoring of temporal variability in coastal water turbidity, Journal of Geophysical Research: Oceans, 117, C9, 2012.

Choi, M., Kim, J., Lee, J., Kim, M., Park, Y.-J., Jeong, U., Kim, W., Hong, H., Holben, B. N., Eck, T. F., Song, C. H., Lim, J.-H., and Song, C.-K.: GOCI Yonsei Aerosol Retrieval (YAER) algorithm and validation during the DRAGON-NE Asia 2012 campaign, Atmos. Meas. Tech., 9, 1377-1398, 2016.

Choi, M., Kim, J., Lee, J., Kim, M., Park, Y.-J., Holben, B., Eck, T. F., Li, Z., and Song, C. H.: GOCI Yonsei aerosol retrieval version 2 products: an improved algorithm and error analysis with uncertainty estimation from 5-year validation over East Asia, Atmospheric Measurement Techniques, 11, 385-408, 2018.

Cox, C.: Statistics of the sea surface derived from sun glitter, J. Marine Research, 13, 198-227, 1954.

Fukuda, S., Nakajima, T., Takenaka, H., Higurashi, A., Kikuchi, N., Nakajima, T. Y., and Ishida, H.: New approaches to removing cloud shadows and evaluating the 380 nm surface reflectance for improved aerosol optical thickness retrievals from the GOSAT/TANSO-Cloud and Aerosol Imager, Journal of Geophysical Research: Atmospheres, 118, 13,520-513,531, 2013.

Garay, M. J., Kalashnikova, O. V., and Bull, M. A.: Development and assessment of a higher-spatial-resolution (4.4 km) MISR aerosol optical depth product using AERONET-DRAGON data, Atmospheric Chemistry and Physics, 17, 5095-5106, 2017.

Garay, M. J., Witek, M. L., Kahn, R. A., Seidel, F. C., Limbacher, J. A., Bull, M. A., Diner, D. J., Hansen, E. G., Kalashnikova, O. V., Lee, H., Nastan, A. M., and Yu, Y.: Introducing the 4.4 km spatial resolution Multi-Angle Imaging SpectroRadiometer (MISR) aerosol product, Atmospheric Measurement Techniques, 13, 593-628, 2020.

Giles, D. M., Sinyuk, A., Sorokin, M. S., Schafer, J. S., Smirnov, A., Slutsker, I., Eck, T. F., Holben, B. N., Lewis, J., Campbell, J., Welton, E. J., Korkin, S., and Lyapustin, A.: Advancements in the Aerosol Robotic Network (AERONET)
570   Version 3 Database – Automated Near Real-Time Quality Control Algorithm with Improved Cloud Screening for Sun Photometer Aerosol Optical Depth (AOD) Measurements, Atmos. Meas. Tech. Discuss., doi: https://doi.org/10.5194/amt-2018-272, 2018. 2018.

Go, S., Kim, J., Park, S. S., Kim, M., Lim, H., Kim, J.-Y., Lee, D.-W., and Im, J.: Synergistic Use of Hyperspectral UV-Visible OMI and Broadband Meteorological Imager MODIS Data for a Merged Aerosol Product, Remote Sensing, 12, 2020.
575

Gupta, P., Patadia, F., and Christopher, S. A.: Multisensor Data Product Fusion for Aerosol Research, IEEE Transactions on Geoscience and Remote Sensing, 46, 1407-1415, 2008.

Gupta, P., Levy, R. C., Mattoo, S., Remer, L. A., and Munchak, L. A.: A surface reflectance scheme for retrieving aerosol optical depth over urban surfaces in MODIS Dark Target retrieval algorithm, Atmospheric Measurement Techniques, 9,
580   3293-3308, 2016.

Gupta, P., Levy, R. C., Mattoo, S., Remer, L. A., Holz, R. E., and Heidinger, A. K.: Applying the Dark Target aerosol algorithm with Advanced Himawari Imager observations during the KORUS-AQ field campaign, 2019. 2019.

Herman, J., Bhartia, P., Torres, O., Hsu, C., Seftor, C., and Celarier, E.: Global distribution of UV-absorbing aerosols from Nimbus 7/TOMS data, Journal of Geophysical Research: Atmospheres, 102, 16911-16922, 1997.

585   Holben, B. N., Tanre, D., Smirnov, A., Eck, T., Slutsker, I., Abuhassan, N., Newcomb, W., Schafer, J., Chatenet, B., and Lavenu, F. J. J. o. G. R. A.: An emerging ground-based aerosol climatology: Aerosol optical depth from AERONET, 106, 12067-12097, 2001.

Hsu, N. C., Tsay, S.-C., King, M. D., Herman, J. R. J. I. T. o. G., and Sensing, R.: Aerosol properties over bright-reflecting source regions, 42, 557-569, 2004.

590   Hsu, N., Jeong, M. J., Bettenhausen, C., Sayer, A., Hansell, R., Seftor, C., Huang, J., and Tsay, S. C.: Enhanced Deep Blue aerosol retrieval algorithm: The second generation, Journal of Geophysical Research: Atmospheres, 118, 9296-9315, 2013.

Hsu, N., Lee, J., Sayer, A., Kim, W., Bettenhausen, C., and Tsay, S. C. J. J. o. G. R. A.: VIIRS Deep Blue aerosol products over land: Extending the EOS long-term aerosol data records, 124, 4026-4053, 2019.

Jackson, J. M., Liu, H., Laszlo, I., Kondragunta, S., Remer, L. A., Huang, J., and Huang, H.-C.: Suomi-NPP VIIRS aerosol
595   algorithms and data products, Journal of Geophysical Research: Atmospheres, 118, 12,673-612,689, 2013.

Kikuchi, M., Murakami, H., Suzuki, K., Nagao, T. M., and Higurashi, A.: Improved Hourly Estimates of Aerosol Optical Thickness Using Spatiotemporal Variability Derived From Himawari-8 Geostationary Satellite, IEEE Transactions on Geoscience and Remote Sensing, 56, 3442-3455, 2018.

Kim, J., Lee, J., Lee, H. C., Higurashi, A., Takemura, T., and Song, C. H., Consistency of the aerosol type classification
600   from satellite remote sensing during the Atmospheric Brown Cloud–East Asia Regional Experiment campaign, J. Geophys. Res., 112, D22S33, doi:10.1029/2006JD008201, 2007.

Kim, J., Yoon, J. M., Ahn, M. H., Sohn, B. J., and Lim, H. S.: Retrieving aerosol optical depth using visible and mid-IR channels from geostationary satellite MTSAT-1R, International Journal of Remote Sensing, 29, 6181-6192, 2008.

Kim, J., Kim, M., and Choi, M.: Monitoring aerosol properties in east Asia from geostationary orbit: GOCI, MI and GEMS.
605   In: Air Pollution in Eastern Asia: An Integrated Perspective, Springer, 2017.

Kim, J., Jeong, U., Ahn, M.-H., Kim, J. H., Park, R. J., Lee, H., Song, C. H., Choi, Y.-S., Lee, K.-H., Yoo, J.-M., Jeong, M.-J., Park, S. K., Lee, K.-M., Song, C.-K., Kim, S.-W., Kim, Y. J., Kim, S.-W., Kim, M., Go, S., Liu, X., Chance, K., Chan Miller, C., Al-Saadi, J., Veihelmann, B., Bhartia, P. K., Torres, O., Abad, G. G., Haffner, D. P., Ko, D. H., Lee, S. H., Woo, J.-H., Chong, H., Park, S. S., Nicks, D., Choi, W. J., Moon, K.-J., Cho, A., Yoon, J., Kim, S.-k., Hong, H., Lee, K., Lee, H.,
610   Lee, S., Choi, M., Veefkind, P., Levelt, P. F., Edwards, D. P., Kang, M., Eo, M., Bak, J., Baek, K., Kwon, H.-A., Yang, J., Park, J., Han, K. M., Kim, B.-R., Shin, H.-W., Choi, H., Lee, E., Chong, J., Cha, Y., Koo, J.-H., Irie, H., Hayashida, S., Kasai, Y., Kanaya, Y., Liu, C., Lin, J., Crawford, J. H., Carmichael, G. R., Newchurch, M. J., Lefer, B. L., Herman, J. R., Swap, R. J., Lau, A. K. H., Kurosu, T. P., Jaross, G., Ahlers, B., Dobber, M., McElroy, C. T., and Choi, Y.: New Era of Air Quality Monitoring from Space: Geostationary Environment Monitoring Spectrometer (GEMS), Bulletin of the American
615   Meteorological Society, 101, E1-E22, 2020.

Kim, M., Kim, J., Wong, M. S., Yoon, J., Lee, J., Wu, D., Chan, P. W., Nichol, J. E., Chung, C.-Y., and Ou, M.-L.: Improvement of aerosol optical depth retrieval over Hong Kong from a geostationary meteorological satellite using critical reflectance with background optical depth correction, Remote Sensing of Environment, 142, 176-187, 2014.

Kim, M., Kim, J., Jeong, U., Kim, W., Hong, H., Holben, B., Eck, T. F., Lim, J. H., Song, C. K., Lee, S., and Chung, C. Y.:
620   Aerosol optical properties derived from the DRAGON-NE Asia campaign, and implications for a single-channel algorithm to retrieve aerosol optical depth in spring from Meteorological Imager (MI) on-board the Communication, Ocean, and Meteorological Satellite (COMS), Atmos. Chem. Phys., 16, 1789-1808, 2016.

Kim, M., Kim, S. H., Kim, W. V., Lee, Y. G., Kim, J., and Kafatos, M. C.: Assessment of Aerosol optical depth under background and polluted conditions using AERONET and VIIRS datasets, Atmospheric Environment, 245, 2021.
625   Knapp, K. R. J. J. o. G. R. A.: Quantification of aerosol signal in GOES 8 visible imagery over the United States, 107, AAC 4-1-AAC 4-11, 2002.

Knapp, K. R., Frouin, R., Kondragunta, S., and Prados, A.: Toward aerosol optical depth retrievals over land from GOES visible radiances: determining surface reflectance, International Journal of Remote Sensing, 26, 4097-4116, 2007.

Koelemeijer, R., De Haan, J., and Stammes, P.: A database of spectral surface reflectivity in the range 335–772 nm derived
630   from 5.5 years of GOME observations, Journal of Geophysical Research: Atmospheres, 108, 2003.

Lee, J., Kim, J., Song, C. H., Ryu, J.-H., Ahn, Y.-H., and Song, C.: Algorithm for retrieval of aerosol optical properties over the ocean from the Geostationary Ocean Color Imager, Remote Sensing of Environment, 114, 1077-1088, 2010.

Lee, J., Kim, J., Yang, P., and Hsu, N. C.: Improvement of aerosol optical depth retrieval from MODIS spectral reflectance over the global ocean using new aerosol models archived from AERONET inversion data and tri-axial ellipsoidal dust
635   database, Atmospheric Chemistry and Physics, 12, 7087-7102, 2012.

Levy, R. C., Remer, L. A., Kleidman, R. G., Mattoo, S., Ichoku, C., Kahn, R., and Eck, T. F.: Global evaluation of the Collection 5 MODIS dark-target aerosol products over land, Atmospheric Chemistry and Physics, 10, 10399-10420, 2010.

Levy, R. C., Mattoo, S., Munchak, L. A., Remer, L. A., Sayer, A. M., Patadia, F., and Hsu, N. C.: The Collection 6 MODIS aerosol products over land and ocean, Atmospheric Measurement Techniques, 6, 2989-3034, 2013.

640   Lee, S., Kim, M., Choi, M., Go, S., Kim, J., Kim, J.-H., Lim, H.-K., Jeong, U., Goo, T.-Y., Kuze, A., Shiomi, K., and Tatsuya, Y.: Aerosol Property Retrieval Algorithm over Northeast Asia from TANSO-CAI Measurements Onboard GOSAT, Remote Sensing, 9, 2017.

Lee, S., Kim, J., Choi, M., Hong, J., Lim, H., Eck, T. F., Holben, B. N., Ahn, J.-Y., Kim, J., and Koo, J.-H.: Analysis of
645   long-range transboundary transport (LRTT) effect on Korean aerosol pollution during the KORUS-AQ campaign, Atmospheric Environment, 204, 53-67, 2019.

Li, L., Shi, R., Zhang, L., Zhang, J., and Gao, W.: The data fusion of aerosol optical thickness using universal kriging and stepwise regression in East China, 2014, 922112.

650 Lim, H., Choi, M., Kim, M., Kim, J., and Chan, P. W.: Retrieval and Validation of Aerosol Optical Properties Using Japanese Next Generation Meteorological Satellite, Himawari-8, Korean Journal of Remote Sensing, 32, 681-691, 2016.

Lim, H., Choi, M., Kim, J., Kasai, Y., and Chan, P.: AHI/Himawari-8 Yonsei Aerosol Retrieval (YAER): Algorithm, Validation and Merged Products, Remote Sens., 10, 2018.

Lyapustin, A., Martonchik, J., Wang, Y., Laszlo, I., and Korkin, S.: Multiangle implementation of atmospheric correction 655 (MAIAC): 1. Radiative transfer basis and look-up tables, Journal of Geophysical Research, 116, 2011a.

Lyapustin, A., Wang, Y., Laszlo, I., Kahn, R., Korkin, S., Remer, L., Levy, R., and Reid, J. S.: Multiangle implementation of atmospheric correction (MAIAC): 2. Aerosol algorithm, Journal of Geophysical Research, 116, 2011b.

Lyapustin, A., Wang, Y., Korkin, S., and Huang, D.: MODIS Collection 6 MAIAC algorithm, Atmospheric Measurement Techniques, 11, 5741-5765, 2018.

660 Mélin, F., Zibordi, G., and Djavidnia, S.: Development and validation of a technique for merging satellite derived aerosol optical depth from SeaWiFS and MODIS, Remote Sensing of Environment, 108, 436-450, 2007.

Murakami, H.: Ocean color estimation by Himawari-8/AHI, 2016, 987810.

Negi, H. and Kokhanovsky, A. J. T. C.: Retrieval of snow albedo and grain size using reflectance measurements in Himalayan basin, 5, 203, 2011.

665 Nguyen, H., Cressie, N., and Braverman, A.: Spatial Statistical Data Fusion for Remote Sensing Applications, Journal of the American Statistical Association, 107, 1004-1018, 2012.

Nirala, M.: Technical Note: Multi-sensor data fusion of aerosol optical thickness, International Journal of Remote Sensing, 29, 2127-2136, 2008.

Pang, J., Liu, Z., Wang, X., Bresch, J., Ban, J., Chen, D., and Kim, J.: Assimilating AOD retrievals from GOCI and VIIRS to 670 forecast surface PM2.5 episodes over Eastern China, Atmospheric Environment, 179, 288-304, 2018.

Remer, L. A., Kaufman, Y., Tanré, D., Mattoo, S., Chu, D., Martins, J. V., Li, R.-R., Ichoku, C., Levy, R., and Kleidman, R.: The MODIS aerosol algorithm, products, and validation, Journal of the atmospheric sciences, 62, 947-973, 2005.

Remer, L. A., Mattoo, S., Levy, R. C., and Munchak, L.: MODIS 3 km aerosol product: algorithm and global perspective, Atmospheric Measurement Techniques Discussions, 6, 69-112, 2013.

675 Saide, P. E., Kim, J., Song, C. H., Choi, M., Cheng, Y., and Carmichael, G. R.: Assimilation of next generation geostationary aerosol optical depth retrievals to improve air quality simulations, Geophysical Research Letters, 41, 9188-9196, 2014.

Saide, P. E., Gao, M., Lu, Z., Goldberg, D., Streets, D. G., Woo, J.-H., Beyersdorf, A., Corr, C. A., Thornhill, K. L., Anderson, B., Hair, J. W., Nehrir, A. R., Diskin, G. S., Jimenez, J. L., Nault, B. A., Campuzano-Jost, P., Dibb, J., Heim, E., Lamb, K. D., Schwarz, J. P., Perring, A. E., Kim, J., Choi, M., Holben, B., Pfister, G., Hodzic, A., Carmichael, G. R., 680 Emmons, L., and Crawford, J. H. : Understanding and improving model representation of aerosol optical properties for a Chinese haze event measured during KORUS-AQ, Atmospheric Chemistry and Physics, 20, 6455-6478,2020.

Sayer, A. M., Hsu, N. C., Bettenhausen, C., and Jeong, M. J.: Validation and uncertainty estimates for MODIS Collection 6 "Deep Blue" aerosol data, Journal of Geophysical Research: Atmospheres, 118, 7864-7872, 2013.

685   Sayer, A., Munchak, L., Hsu, N., Levy, R., Bettenhausen, C., and Jeong, M. J.: MODIS Collection 6 aerosol products: Comparison between Aqua's e-Deep Blue, Dark Target, and "merged" data sets, and usage recommendations, Journal of Geophysical Research: Atmospheres, 119, 2014.

Sayer, A., Hsu, N., Lee, J., Bettenhausen, C., Kim, W., and Smirnov, A. J. J. o. G. R. A.: Satellite Ocean Aerosol Retrieval (SOAR) Algorithm Extension to S-NPP VIIRS as Part of the "Deep Blue" Aerosol Project, 123, 380-400, 2018.

690   Sayer, A. M., Hsu, N. C., Lee, J., Kim, W. V., and Dutcher, S. T.: Validation, Stability, and Consistency of MODIS Collection 6.1 and VIIRS Version 1 Deep Blue Aerosol Data Over Land, Journal of Geophysical Research: Atmospheres, 124, 4658-4688, 2019.

Smirnov, A., Holben, B. N., Eck, T. F., Dubovik, O., and Slutsker, I.: Cloud screening and quality control algorithms for the AERONET data base, Remote Sens. Environ., 73, 337-349, 2000.

695   Stocker, T. F., Qin, D., Plattner, G.-K., Tignor, M., Allen, S. K., Boschung, J., Nauels, A., Xia, Y., Bex, B., and Midgley, B.: IPCC, 2013: climate change 2013: the physical science basis. Contribution of working group I to the fifth assessment report of the intergovernmental panel on climate change. Cambridge University Press, 2013.

Tang, Q., Bo, Y., and Zhu, Y.: Spatiotemporal fusion of multiple-satellite aerosol optical depth (AOD) products using Bayesian maximum entropy method, Journal of Geophysical Research: Atmospheres, 121, 4034-4048, 2016.

700   Wang, J.: Geostationary satellite retrievals of aerosol optical thickness during ACE-Asia, Journal of Geophysical Research, 108, 2003.

Wang, J., Brown, D. G., and Hammerling, D.: Geostatistical inverse modeling for super-resolution mapping of continuous spatial processes, Remote Sensing of Environment, 139, 205-215, 2013.

Wei, J., Li, Z., Sun, L., Peng, Y., and Wang, L.: Improved merge schemes for MODIS Collection 6.1 Dark Target and Deep
705   Blue combined aerosol products, Atmospheric Environment, 202, 315-327, 2019.Xie, Y., Xue, Y., Che, Y., Guang, J., Mei, L., Voorhis, D., Fan, C., She, L., Xu, H. J. I. T. o. G., and Sensing, R.: Ensemble of ESA/AATSR aerosol optical depth products based on the likelihood estimate method with uncertainties, 56, 997-1007, 2018.

Xu, H., Guang, J., Xue, Y., De Leeuw, G., Che, Y., Guo, J., He, X., and Wang, T. J. A. E.: A consistent aerosol optical depth (AOD) dataset over mainland China by integration of several AOD products, 114, 48-56, 2015.

710   Xue, Y., Xu, H., Mei, L., Guang, J., Guo, J., Li, Y., Hou, T., Li, C., Yang, L., He, X. J. A. C., and Discussions, P.: Merging aerosol optical depth data from multiple satellite missions to view agricultural biomass burning in Central and East China, 12, 10461-10492, 2012.

Yoon, J. M., Kim, J., Lee, J. H., Cho, H. K., Sohn, B.-J., and Ahn, M.-H. J. A.-P. J. o. A. S.: Retrieval of aerosol optical
715   depth over East Asia from a geostationary satellite, MTSAT-1R, 43, 49-58, 2007.

Yoshida, M., Kikuchi, M., Nagao, T. M., Murakami, H., Nomaki, T., and Higurashi, A.: Common Retrieval of Aerosol Properties for Imaging Satellite Sensors, Journal of the Meteorological Society of Japan. Ser. II, 96B, 193-209, 2018.

Zhong, G., Wang, X., Tani, H., Guo, M., Chittenden, A., Yin, S., Sun, Z., and Matsumura, S.: A Modified Aerosol Free Vegetation Index Algorithm for Aerosol Optical Depth Retrieval Using GOSAT TANSO-CAI Data, Remote Sensing, 8,
720   2016.

Table 1. Satellite dataset used for the fusion products.

AOD type	F1	F2	F3	F4	FM1	FM2	FM3
AER	o	o	o	o	o	o	o
AMR	o		o	o	o		o
GV1	o				o		
GV2	o	o		o	o	o	
Remark				Without GV1 to check missing effect	MLE Products[2]		
	All available products	For NRT[1]	AHI only for wider area		Same as F1	Same as F2	Same as F3

[1] NRT: near real time; [2] Maximum Likelihood Estimation
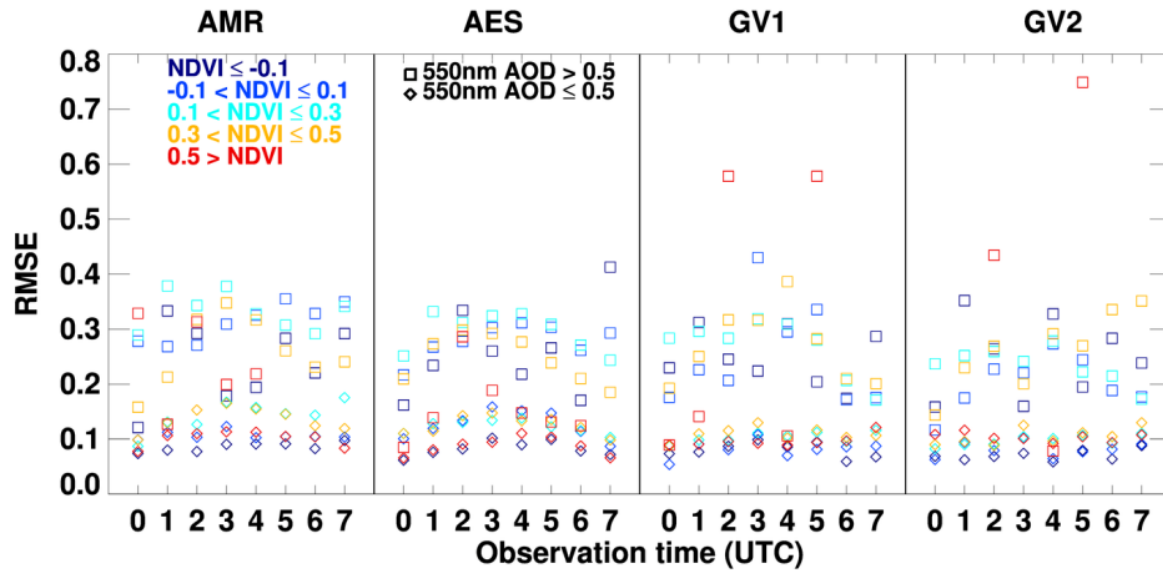
Figure 1. RMSE according to NDVI (color), observation time, and satellite AODs (square and diamond represent AOD at 550nm greater and less equal than 0.5) during Apr. 2018 to Mar. 2019 excluding EMeRGe campaign.
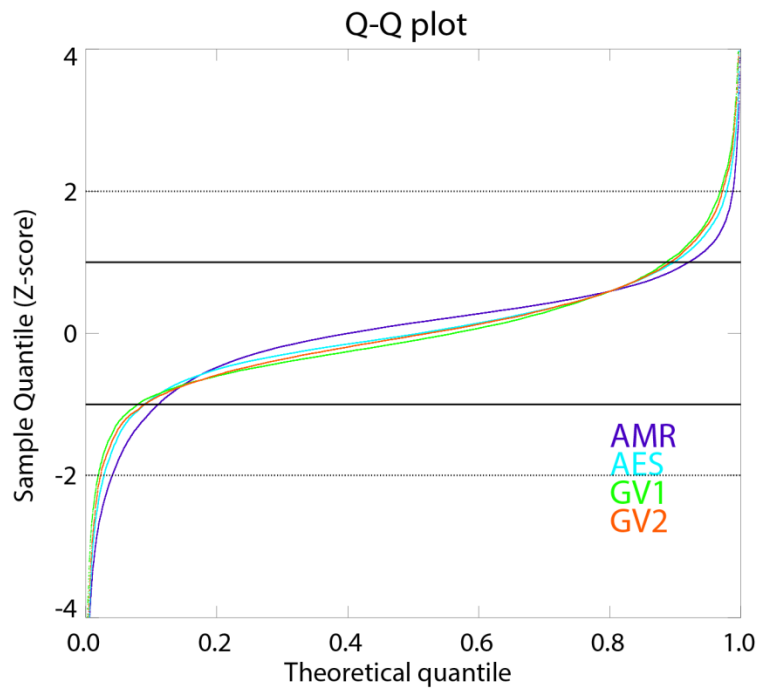
Figure 2. Q-Q plot for the difference between AERONET AOD and AMR(purple), AES(cyan), GV1(green), and GV2(orange) AOD. The black solid line and dotted line represent 1-σ and 2-σ, respectively.
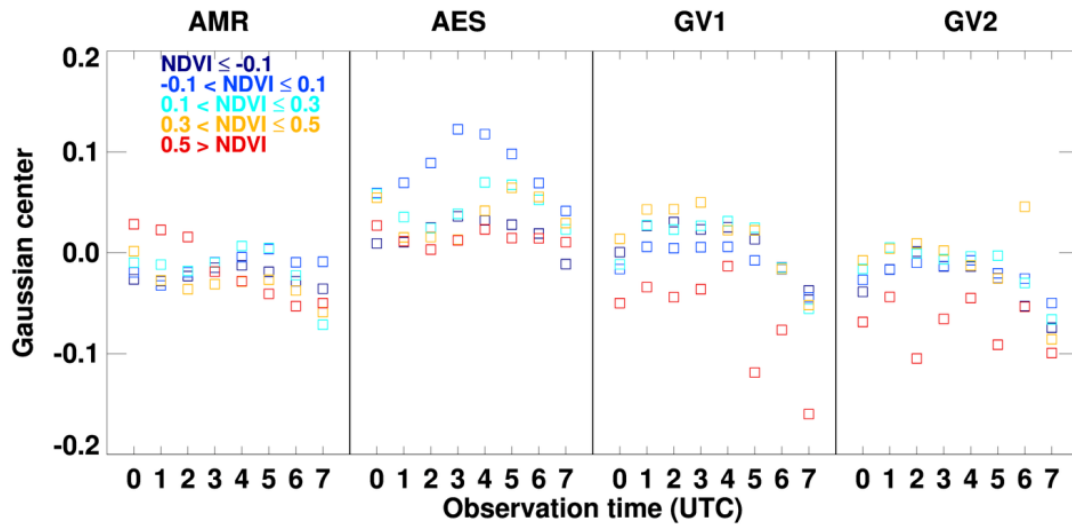
Figure 3. Systematic bias-correction values for NDVI groups and temporal bins for each satellite product from Gaussian fitting analysis used in MLE fusion.
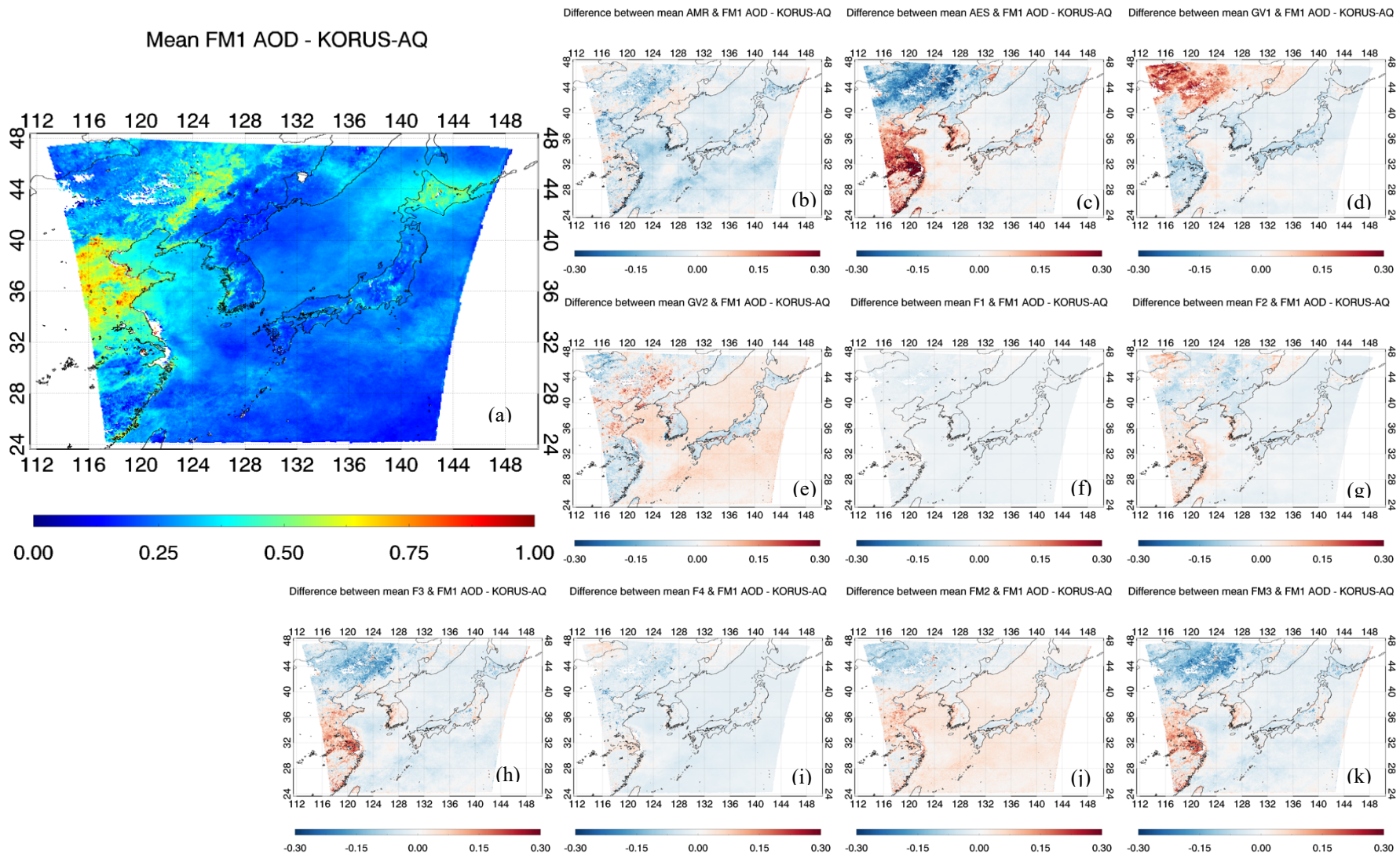
Figure 4. The average AOD of (a) FM1 (AMR, AES, GV1, and GV2) during the KORUS AQ. The difference of mean (b)AMR, (c)AES, (d)GV1, (e)GV2, (f)F1,(g)F2, (h)F3, (i)F4, (j)FM2, and (k)FM3 AODs with respect to mean representative (FM1) AOD. Figures generated with Interactive Data Language (IDL) version 8.8.0.
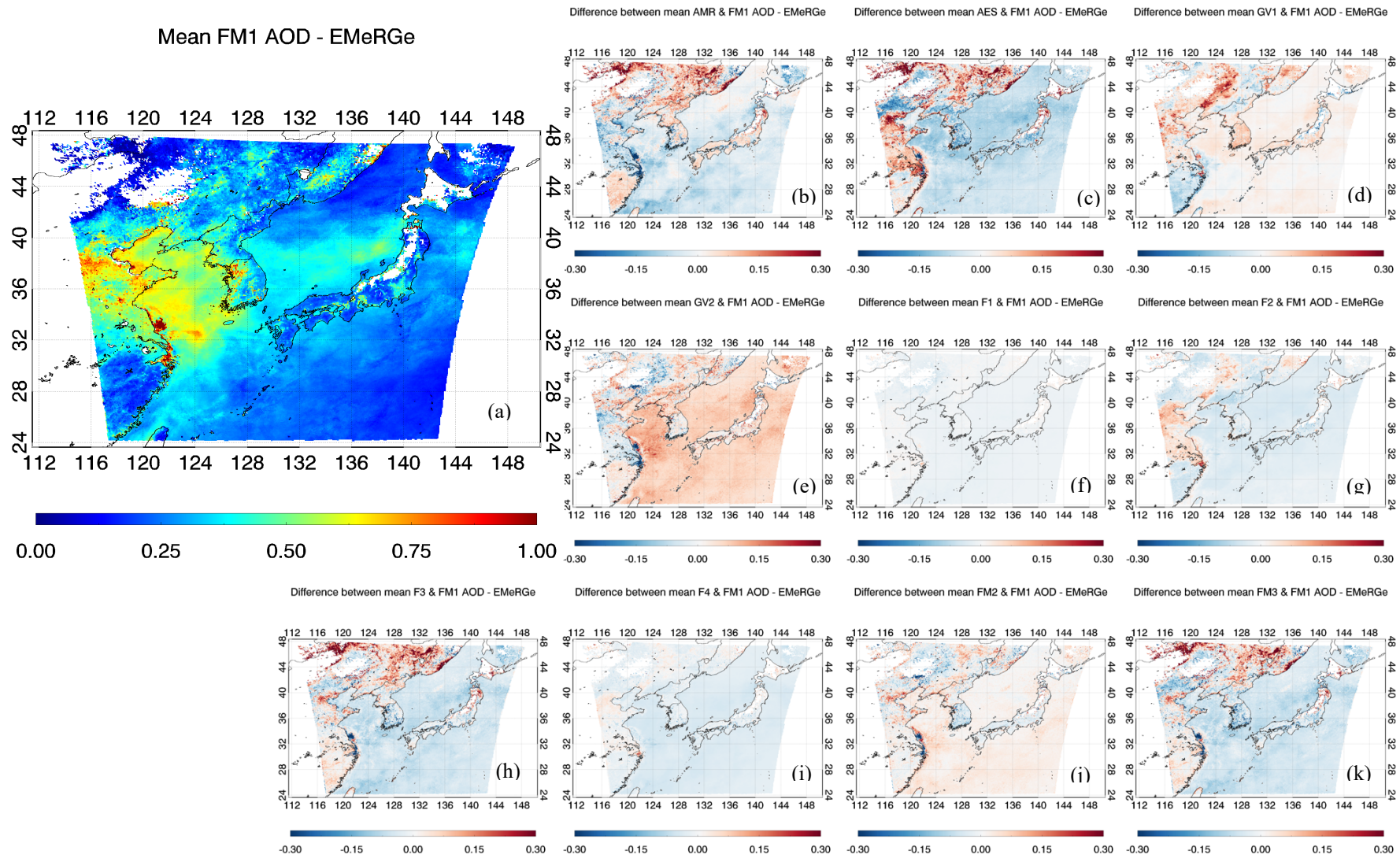
Figure 5. Same as Figure 4, but for EMeRGe campaign.
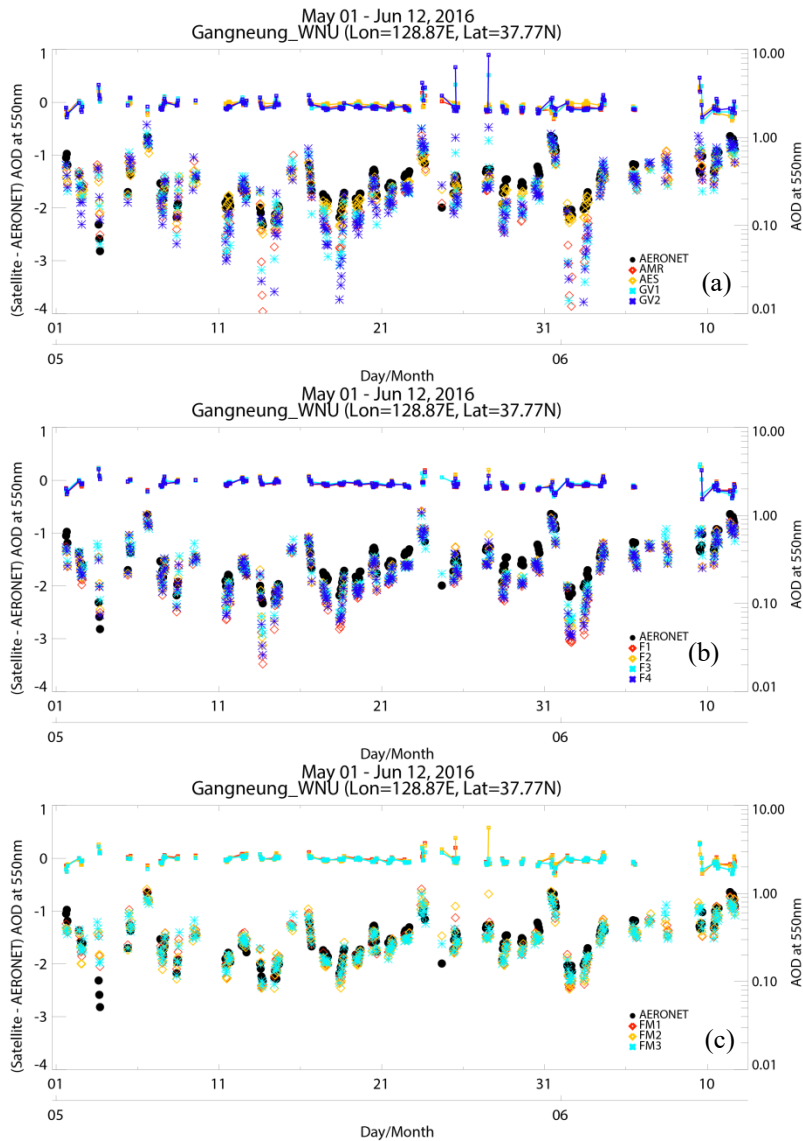
Figure 6. Time series of the AODs at Gangneung WNU site during the KORUS-AQ campaign from (a) respective satellite, (b) ensemble-mean, and (c) MLE fusion (to the right y-axis). Solid line represents difference of individual satellite retrieval from AERONET AOD at 550nm (to the left y-axis).
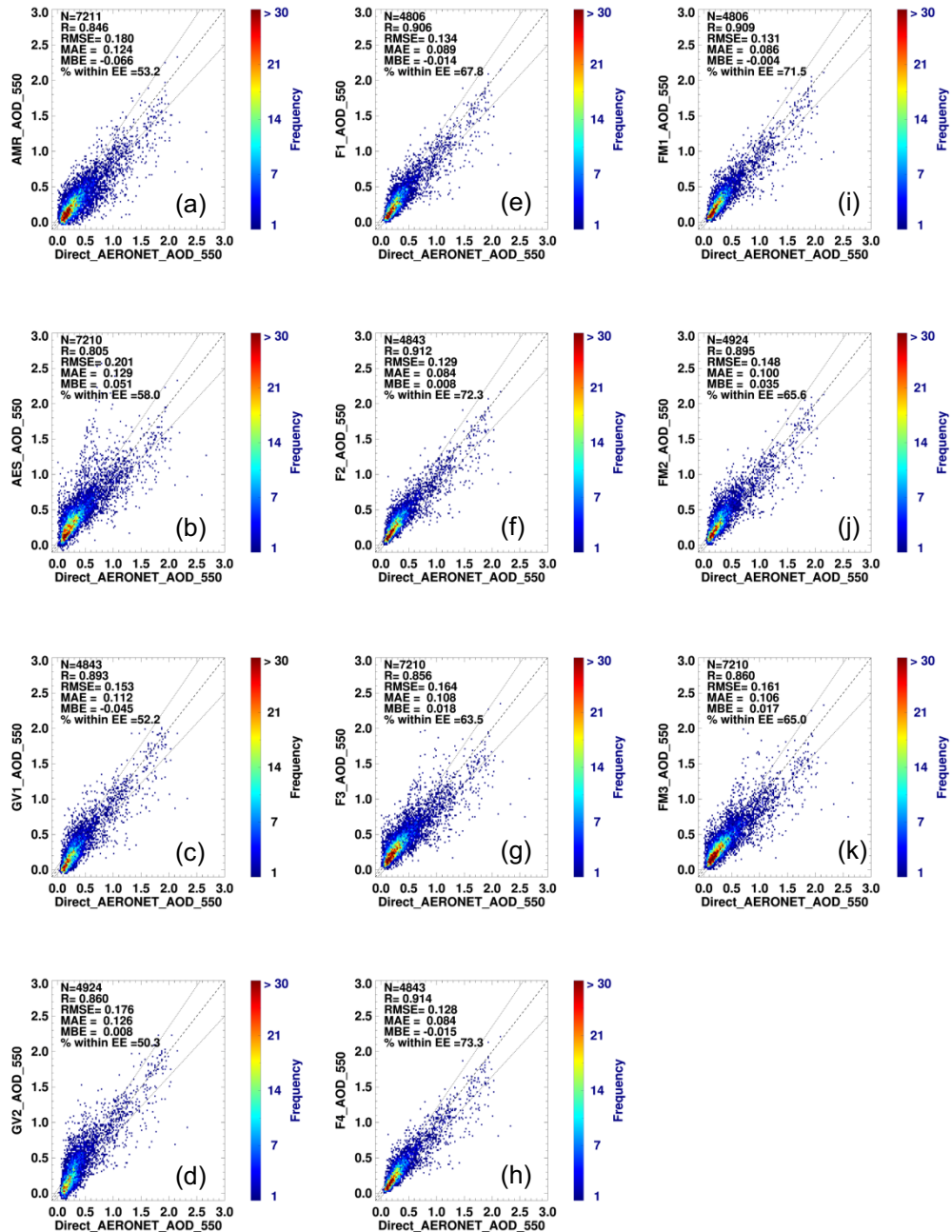
Figure 7. Comparison of four respective satellite products (a) AMR, (b) AES, (c) GV1, (d) GV2, four ensemble mean products (e) F1, (f) F2, (g) F3, (h) F4, and three MLE products (i) FM1, (j) FM2, (k)FM3 AOD with AERONETAOD during KORUS-AQ campaign.
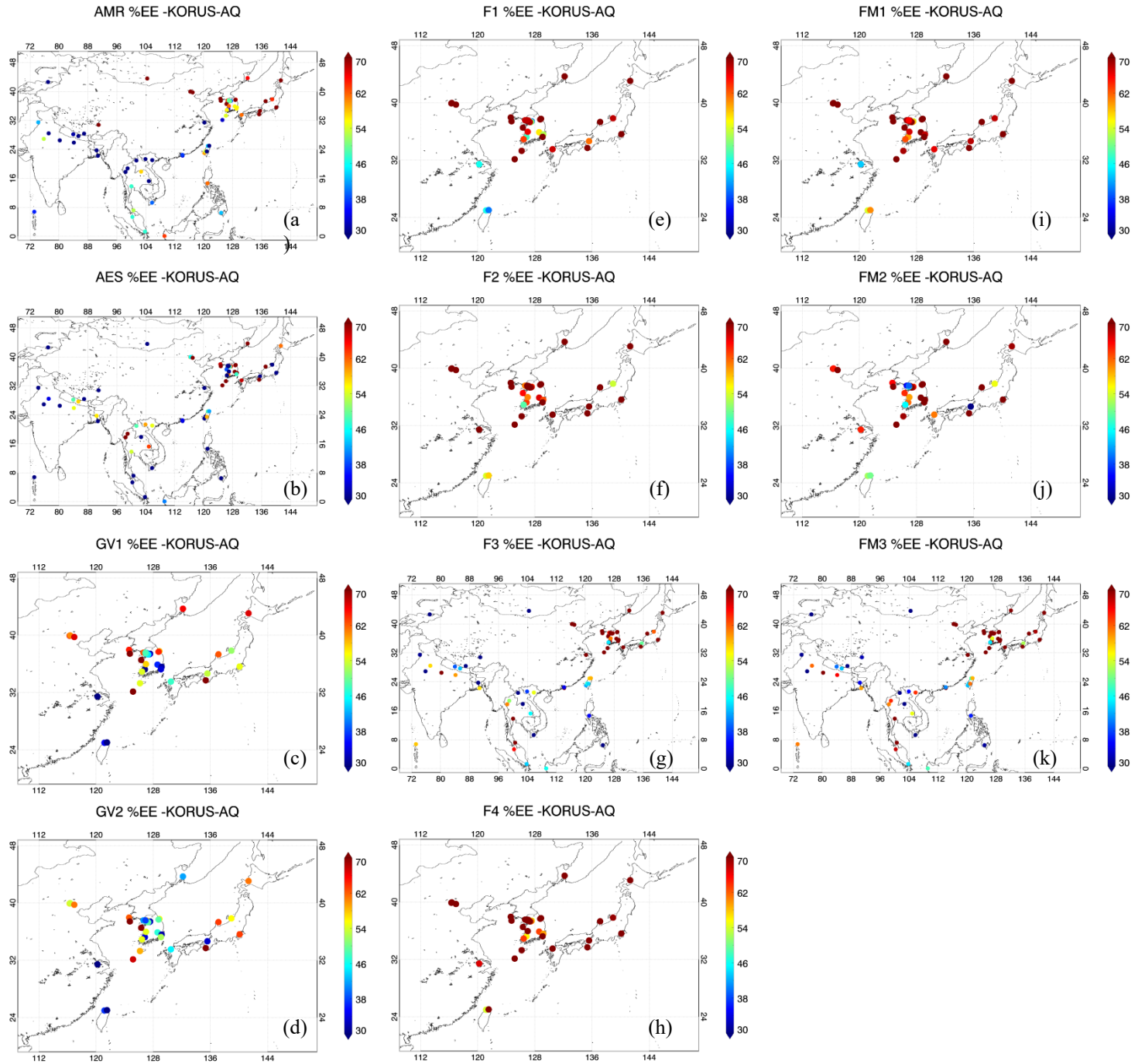
Figure 8. Spatial distribution of %EE for (a) AMR, (b) AES, (c) GV1, (d) GV2, (e) F1, (f) F2, (g) F3, (h) F4, (i) FM1, (j) FM2, and (k) FM3AOD during the KORUS-AQ campaign. Figures generated with Interactive Data Language (IDL) version 8.8.0.
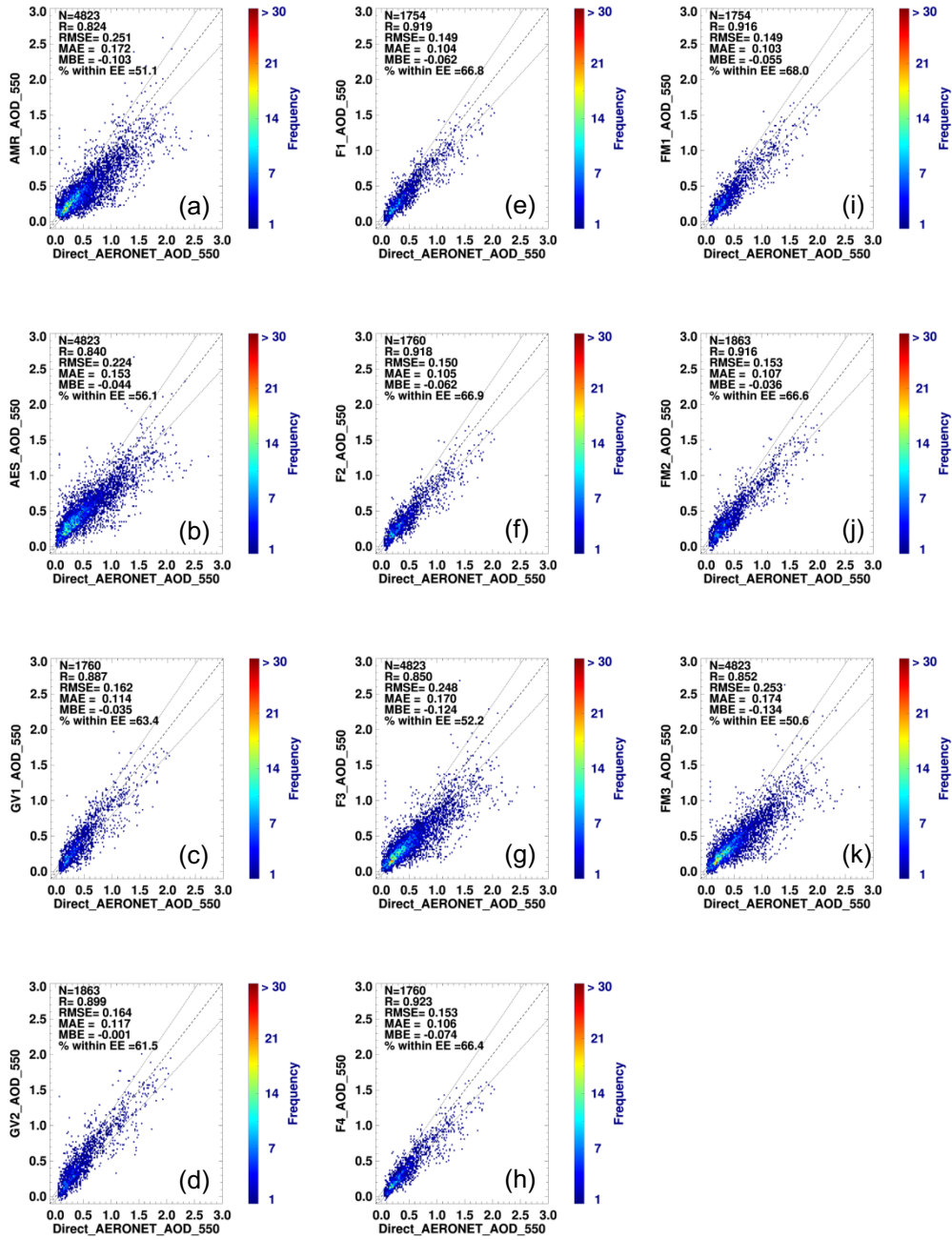
Figure 9. Same as Figure 7, but for EMeRGe campaign.
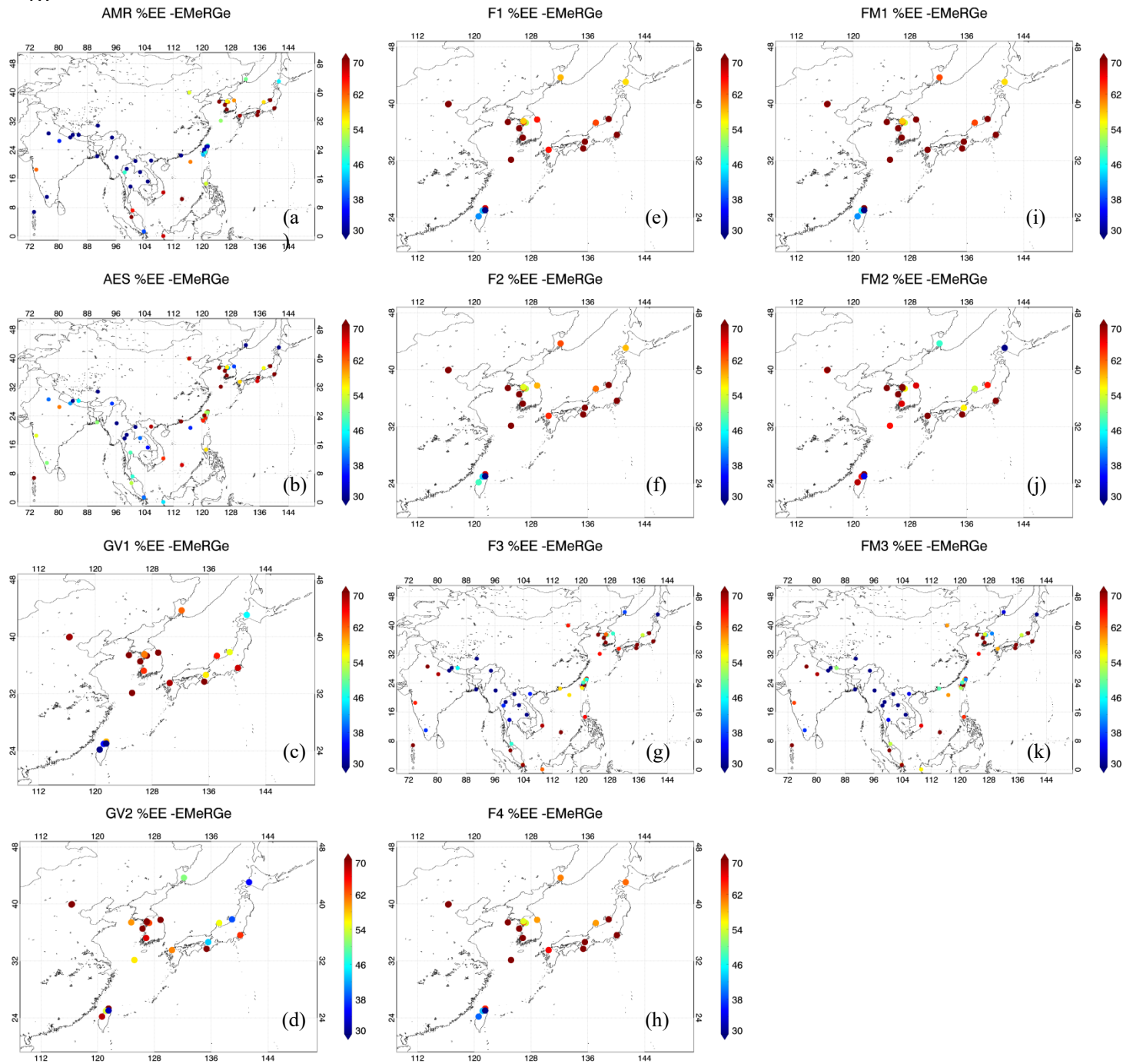
Figure 10. Same as Figure 8, but for the EMeRGe campaign.
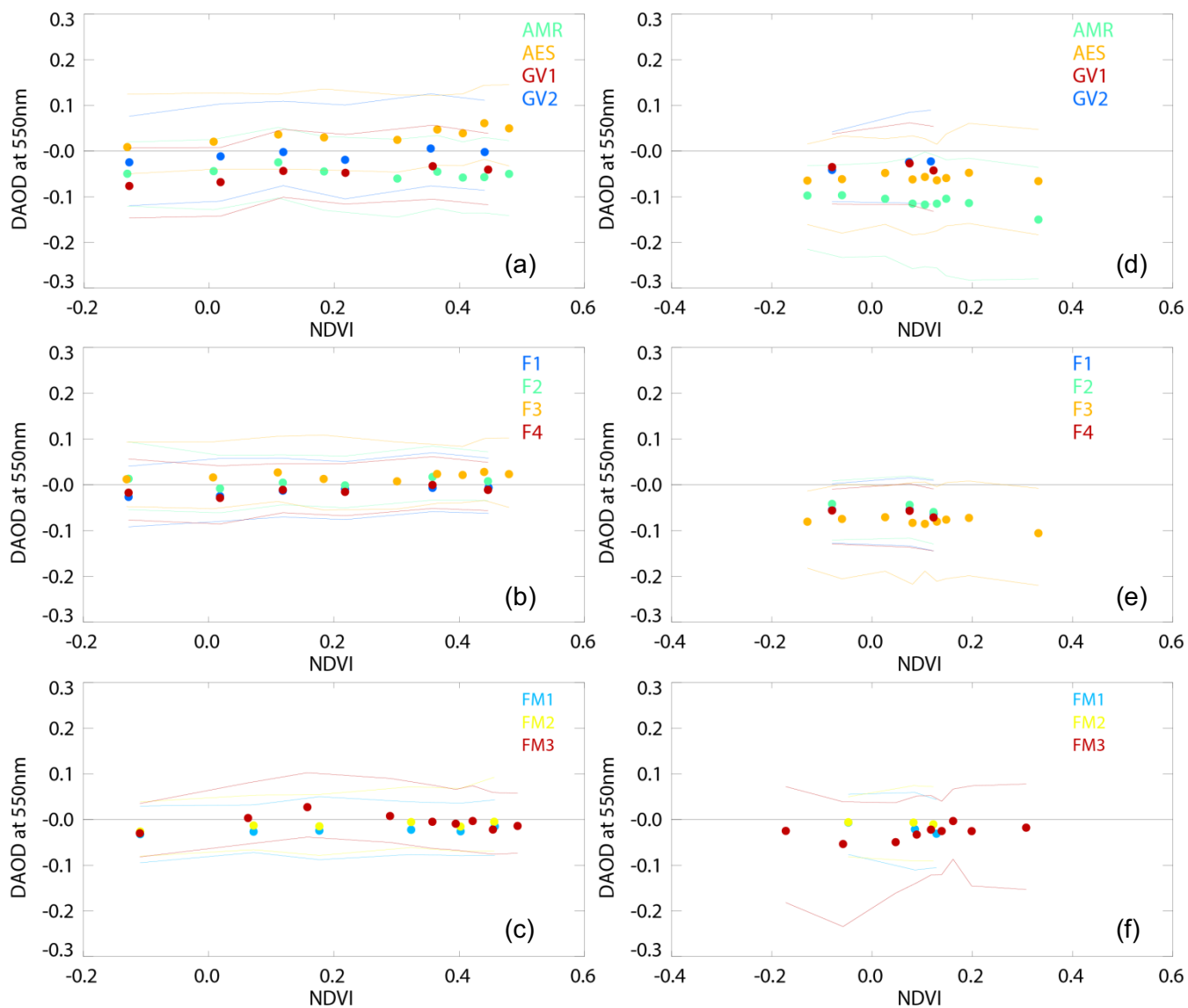
Figure 11. Difference between (a, d) respective, (b, e) ensemble-mean, or (c, f) MLE and AERONET AOD in terms of NDVI during the KORUS-AQ (left column) and the EMeRGe (right column) campaigns. Each points and solid lines represent the median and 1-σ (16th and 84th percentile) of 800 (for the KORUS-AQ) and 600 (for the EMeRGe) collocated data points in terms of NDVI values.
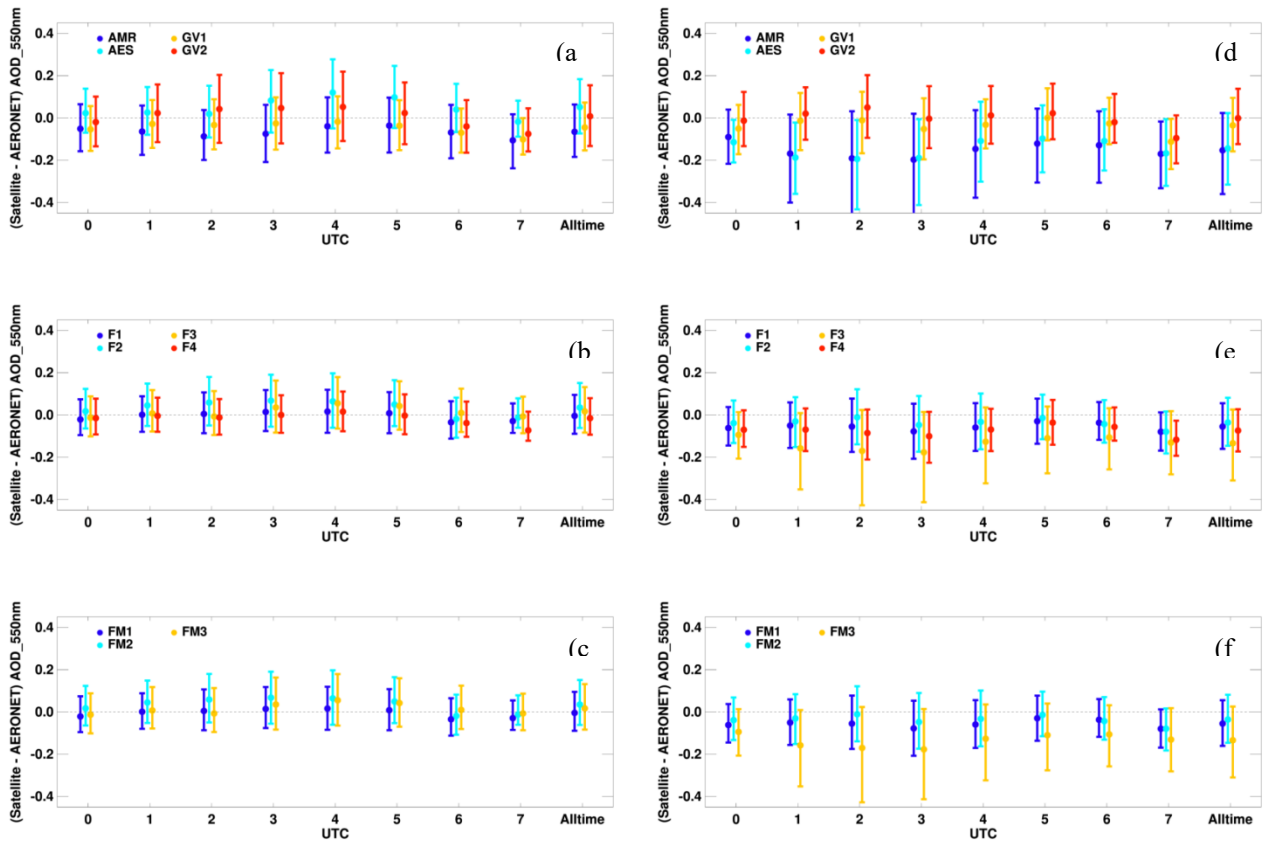
Figure 12. Same as Figure 11, but for the observation time.
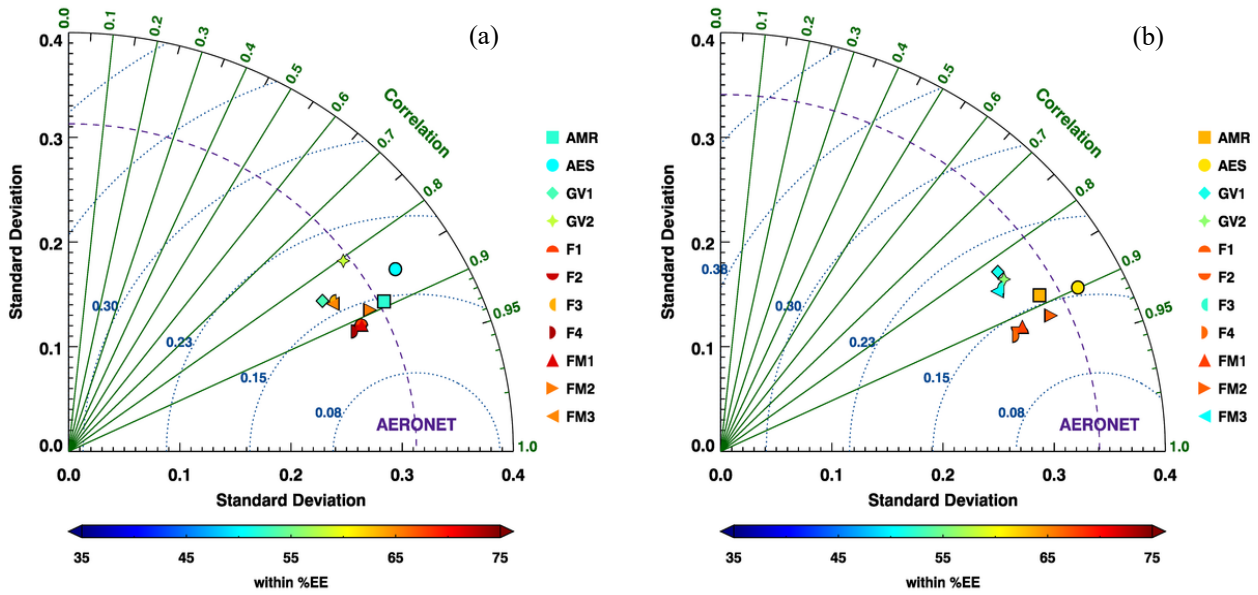
Figure 13. Taylor diagrams comparing the respective, ensemble-mean, and MLE AODs and values obtained from AERONET during the (a) KORUS-AfQ and (b) EMeRGe periods. Square, circle, diamond, star, top half circle, lower half circle, left half circle, right half circle, triangle, right-pointing triangle, and left-pointing triangle represents AMR, AES, GV1, GV2, F1, F2, F3, F4, FM1, FM2, and FM3, respectively.

Table 2. Accuracy evaluation of GOCI area of AMR, AES, F3, and FM3 AODs.

(all / collocation with GOCI domain)	KORUS-AQ AMR	KORUS-AQ AES	KORUS-AQ F3	KORUS-AQ FM3	EMeRGe AMR	EMeRGe AES	EMeRGe F3	EMeRGe FM3
N	7211 / 5069	7210 / 5069	7210 / 5069	7210 / 5069	4823 / 1884	4823 / 1884	4823 / 1884	4823 / 1884
R	0.846 / 0.908	0.805 / 0.905	0.856 / 0.919	0.860 / 0.922	0.824 / 0.910	0.840 / 0.892	0.850 / 0.912	0.253 / 0.911
RMSE	0.180 / 0.150	0.201 /0.145	0.164 / 0.133	0.161 / 0.131	0.251 / 0.162	0.224 / 0.176	0.248 / 0.175	0.253 / 0.184
MBE	-0.066 / -0.054	0.051 /0.029	0.018 / 0.012	0.017 / 0.01	-0.103 / -0.028	-0.044 / -0.011	-0.124 /-0.069	-0.134 / -0.086
%EE	53.2 / 60.6	58.0 /63.5	63.5 / 72.1	65.0 / 72.9	51.1 / 69.4	56.1 / 65.2	52.2 / 63.2	50.6 / 60.0